# Submesoscale effects on changes to export production under global warming

Genevieve Jay Brett[1], Daniel Bridger Whitt[2], Matthew C. Long[3], Frank O. Bryan[3], Kate Feloy[4], and Kelvin J Richards[4]

[1]Johns Hopkins University
[2]NASA Ames Research Center
[3]National Center for Atmospheric Research (UCAR)
[4]University of Hawaii at Manoa

December 7, 2022

**Abstract**

We examine the effects of the submesoscale in mediating the response to projected warming of phytoplankton new production and export using idealized biogeochemical tracers in a high-resolution regional model of the Porcupine Abyssal Plain region of the North Atlantic. We quantify submesoscale effects by comparing our control run to an integration in which submesoscale motions have been suppressed using increased viscosity. The warming climate over the 21st century reduces resolved submesoscale activity by a factor of 2-3. Annual new production is slightly reduced by submesoscale motions in a climate representative of the early 21st-century and slightly increased by submesoscale motions in a climate representative of the late 21st-century. Resolving the submesoscale, however, does not strongly impact the projected reduction in annual production under representative warming. Organic carbon export from the surface ocean includes both direct sinking of detritus (the biological gravitational pump) and advective transport mediated pathways; the sinking component is larger than advectively mediated transport by up to an order of magnitude across a wide range of imposed sinking rates. Submesoscales are responsible for most of the advective carbon export, however, which is thus largely reduced by a warming climate. In summary, our results demonstrate that resolving more of the submesoscale has a modest effect on present-day new production, a small effect on simulated reductions in new production under global warming, and a large effect on advectively-mediated export fluxes.

# Submesoscale effects on changes to export production under global warming


**Genevieve Jay Brett[1,2], Daniel B Whitt[3,4], Matthew C Long[4], Frank O. Bryan[4], Kate Feloy[2], Kelvin J. Richards[2]**

[1]Johns Hopkins University Applied Physics Laboratory 11100 Johns Hopkins Road, Laurel, MD 20723, USA

[2]University of Hawai'i Manoa 1680 East West Road, Honolulu HI 96822, USA

[3]Ames Research Center, National Aeronautics and Space Administration, Moffett Field, CA, USA

[4]Climate and Global Dynamics Laboratory, National Center for Atmospheric Research, Boulder, CO, USA


## Key Points:

- For the Porcupine Abyssal Plain region, submesoscales drive a 3% reduction in annual production in an early 21st-century climate.
- Projected changes in annual production over the 21st century are similar regardless of including submesoscales.
- Including submesoscales increases advectively-mediated carbon export fluxes by 58-70%.

Corresponding author: Jay Brett, `Jay.Brett@jhuapl.edu`

## Abstract

We examine the effects of the submesoscale in mediating the response to projected warming of phytoplankton new production and export using idealized biogeochemical tracers in a high-resolution regional model of the Porcupine Abyssal Plain region of the North Atlantic. We quantify submesoscale effects by comparing our control run to an integration in which submesoscale motions have been suppressed using increased viscosity. The warming climate over the 21st century reduces resolved submesoscale activity by a factor of 2-3. Annual new production is slightly reduced by submesoscale motions in a climate representative of the early 21st-century and slightly increased by submesoscale motions in a climate representative of the late 21st-century. Resolving the submesoscale, however, does not strongly impact the projected reduction in annual production under representative warming. Organic carbon export from the surface ocean includes both direct sinking of detritus (the biological gravitational pump) and advective transport mediated pathways; the sinking component is larger than advectively mediated transport by up to an order of magnitude across a wide range of imposed sinking rates. Submesoscales are responsible for most of the advective carbon export, however, which is thus largely reduced by a warming climate. In summary, our results demonstrate that resolving more of the submesoscale has a modest effect on present-day new production, a small effect on simulated reductions in new production under global warming, and a large effect on advectively-mediated export fluxes.


## Plain Language Summary

We examine the effects of a warming climate on phytoplankton growth and the sinking of organic matter in the ocean using numerical simulations of a region of the northeastern North Atlantic. We quantify the effects of physical motions at scales below 25km (submesoscales) by suppressing them in some simulations. In this region, submesoscale motions are less energetic in the warmer climate at the end of the 21st century. Annual phytoplankton growth is slightly reduced when including these motions in the current climate and slightly increased when including them in the warmer climate. The projected reduction in phytoplankton growth over the 21st century due to a warming climate, however, is not very sensitive to the inclusion of submesoscales in our simulations. The transfer of organic matter from surface to depth is due to both sinking of particles and vertical motions of the water. Submesoscales are responsible for most of vertical transfer of organic matter by vertical water movement, which is largely reduced by a warming climate. Therefore, global climate models that do not explicitly represent the submesoscale are likely to be accurate for phytoplankton growth but not for the downward transport of organic matter.

## 1 Introduction

Global warming over the 21st century is expected to alter the ocean's biological pump, but the sensitivity, and thus magnitude of response, of important rates remain uncertain (Kwiatkowski et al., 2020; Séférian et al., 2020; Henson et al., 2022). The eastern North Atlantic has one of the largest and most robust projected declines in export production under global warming in global Earth system models (Bopp et al., 2013; Kwiatkowski et al., 2020, their figures 9 and 2 respectively). This robustness may be related to consistent projections of reduced mixed layer depths, which suggest a link between increased upper ocean buoyancy stratification and the fluxes of nutrients in the euphotic zone. In the ocean, these mixed layer depths and nutrient fluxes are strongly affected by physical stirring and mixing in the upper ocean, which are sensitive to mesoscale horizontal stirring and submesoscale vertical velocities. However, standard climate projections use global, low-resolution Earth system models (e.g. Fu et al., 2016). Meso- and submesoscale physical processes are not resolved in such projections, so the impact of warming on motions at these scales, and the impact of such changes, is an ongoing area of research.

Submesoscale motions, which have lateral extents of 1–25km and are characterized by large Rossby numbers, sharp fronts, and strong jets, can induce large vertical motions (Capet, McWilliams, et al., 2008b; Klein & Lapeyre, 2009; McWilliams, 2016). These motions can develop due to baroclinic instabilities (Boccaletti et al., 2007; Fox-Kemper et al., 2008; Callies et al., 2016), mesoscale stirring (Lapeyre & Klein, 2006; Roullet et al., 2012), and air-sea interactions (Callies & Ferrari, 2018; Thomas et al., 2008). The induced vertical motions can strongly impact the vertical tracer fluxes of nutrients and biomass, affecting primary production and export (Lévy et al., 2001; Levy, Ferrari, et al., 2012; Lévy et al., 2018; Mahadevan, 2016; Smith et al., 2016; Couespel et al., 2021; Dever et al., 2021). Besides direct impacts on fluxes, submesoscale motions associated with mixed layer baroclinic instabilities (MLI) can lead to restratification of the mixed layer (Fox-Kemper et al., 2008) and a reduction in the mixed layer depth (Karimpour et al., 2018). The strength of MLI depends on horizontal and vertical buoyancy stratification, the latter of which can be approximated by the mixed layer depth (MLD). Realistic regional ocean models have shown that the scaling of MLI strength is a good indicator of submesoscale activity, including seasonal variations associated with the MLD (Capet, McWilliams, et al., 2008a; Capet, Campos, & Paiva, 2008; Mensa et al., 2013) and changes due to global warming (Richards et al., 2021).

Under projected global warming, increased ocean stratification is expected in most regions. This increased stratification leads to shallower winter mixed layers in general, although not all ocean regions have this same response, especially across different models used (Fox-Kemper et al., 2021). In the North Atlantic, however, a shallowing of deep winter mixed layers is consistently projected, owing to both warming and strong freshwater fluxes (Fox-Kemper et al., 2021). The seasonal shifts in mixed layer depth in the North Atlantic has long been considered critical for primary production and its seasonal cycle (Sverdrup, 1953; Behrenfeld & Boss, 2014; Sathyendranath et al., 2015). Richards et al. (2021) show that under a warming scenario that significantly reduces winter MLD in the northeast North Atlantic, there is a substantial reduction in winter submesoscale activity and associated vertical buoyancy fluxes. How such reductions in physical fluxes modify the climate response of primary production and export is the question of interest here.

The impact of submesoscale activity on tracer fluxes and biogeochemical reactions has been undertaken in many recent studies; Mahadevan (2016) and Lévy et al. (2018) provide thorough reviews. One common approach is to simulate a single, persistent front (e.g. Lévy et al., 2001; Mahadevan & Tandon, 2006; Ramachandran et al., 2014; Freilich & Mahadevan, 2019). These efforts show that strong vertical motions and the tilting of isopycnals at these fronts induce large tracer fluxes, generally increasing nutrient supply, production, and advective export rates. Observations of tracer transport at individual submesoscale fronts has generally shown strong vertical motions and advection of tracer filaments as well (Omand et al., 2015; Olita et al., 2017; Ruiz et al., 2019; Archer et al., 2020). Estimating the regional and global impact of submesoscale motions from knowledge of their local significance is difficult, however. This quantification is still only beginning to be performed for heat fluxes (Su et al., 2018).

Quantifying the regionally-integrated impact of submesoscales on nutrient fluxes and production can be done with modeling studies on larger domains with more realistic flows, but there is not yet a consensus on the sign of the effect of resolving the submesoscale. Consistent with studies of individual fronts, models of the Southern Ocean showed that resolving more of the submesoscale increased the upward iron supply such that submesoscales contributed 30% of the total iron flux (Uchida et al., 2019), and doubled production (Uchida et al., 2020). In the Northeast North Atlantic region with mode water formation, resolving submesoscales increased regional production, but only by 5% (Karleskind et al., 2011). Varying resolution of another North Atlantic model showed, in contradiction, that increased resolution can decrease primary production, due to increased stratification that limits nutrient supply (Levy, Iovino, et al., 2012).

Export rates are influenced by many processes, as discussed in Boyd et al. (2019). The biological gravitational pump is the most measured, while the eddy subduction pump is the advective contribution likely affected by submesoscales. Advective export rates can be substantially increased by submesoscale motions at fronts, but the impact can be small compared to the gravitational pump or other terms. Dever et al. (2021) demonstrate that the dominant term between the eddy subduction pump and biological gravitational pump depends on both the submesoscale activity and the gravitational sinking rate, related to the size spectrum of particles exported. Resplandy et al. (2019) saw that intense submesoscale features induced large export fluxes locally in a submesoscale-resolving North Atlantic model, but that they contributed less than 5% of basin-wide export. Similarly, Karleskind et al. (2011) found that advectively-mediated subduction increased by about 10% in the Northeast Atlantic with resolved submesoscales.

In the context of climate projections, submesoscale activity is generally parameterized as a subgrid transport if it is included at all, as resolving the submesoscale (and sometimes the mesoscale) in global models over decades or centuries remains prohibitively expensive (Fox-Kemper et al., 2019). One of many reasons that projections of export production, for example, are so varied is that different models have different subgrid-scale transport (Glessmer et al., 2008; Löptien & Dietze, 2019). Resolving the mesoscale rather than parameterizing it can change production dynamics; in models of upwelling eastern boundary systems, resolved mesoscale eddies reduce production, due to enhanced nutrient transport offshore rather than upward (Lathuiliere et al., 2011; Gruber et al., 2011). For the subpolar North Atlantic, nutrient transport is also critical: D. B. Whitt & Jansen (2020) find that the driver of changes in primary production with warming is the slowing supply of nutrients from lower latitudes due to slowing circulation. However, this analysis does not include explicit vertical transport at mesoscales to submesoscales, which may be an important secondary feedback.

The question remains: how will changes in submesoscale activity in a warming upper ocean affect vertical tracer transport and primary production? Our objective is to quantify the effect of resolving more of the submesoscale on new production and export for an ocean region where global warming is projected to have a substantial impact on submesoscale activity. We use the same northeast North Atlantic region as in Richards et al. (2021), where submesoscale activity is reduced by half as winter mixed layer depths are reduced by 60%. We use the same "time slice" method as in that work to create a model ocean representative of a warmer climate. To suppress submesoscale variability, we increase the viscosity and diffusivity of the flow, rather than changing the model grid. To model new production and export, we use a pair of idealized tracers representing a single nutrient and phytoplankton, similar to G. J. Brett et al. (2021). This design of idealized tracers and submesoscale sensitivity study provides a distinct perspective on how global warming impacts on submesoscale physics and MLD modify production and export, a new window into the uncertain processes of interest. Section 2 describes the physical and biogeochemical model. Section 3 quantifies the impact of submesoscales on reductions of new production under global warming. Section 4 quantifies the contribution of submesoscale advection to export in this scenario.

# 2 Methods

## 2.1 Physical model

Richards et al. (2021) provide details of the nearly identical model setup (with different highest resolution). We briefly summarize the method here and have included more detail in Supplement Section S1. We use the Regional Ocean Modeling System (ROMS, Shchepetkin & McWilliams (2005)) with a 4 km grid to simulate the Porcupine Abyssal Plain region in the North Atlantic, specifically 41-51°N and 11-27°W. This regional model is in a one-way-nested configuration within the ocean component of the Community Earth System Model (CESM) version 2.0 (Lauritzen et al., 2018), integrated at a nominal 0.1° and forced by atmospheric fields representative of a statistically normal annual cycle, i.e. a normal year (Large & Yeager, 2004). We utilize the "time slice" approach for our global model, as described in Richards et al. (2021) and G. J. Brett et al. (2021). Thus, the global model's initial conditions and both models' surface forcing are set to simulate a period representative of either early- or late-century climate conditions, with the adjustments for late-century conditions set by anomalies computed from the fully-coupled CESM1 Large Ensemble (CESM-LE; Kay et al., 2015).

The regional model is initialized with February 1 conditions from the global model and run for 4 years. To suppress a portion of the submesoscale in what we call the *viscous* runs, as opposed to *standard* runs, we increase the viscosity and diffusivity via increasing the hyperdiffusivity and hyperviscosity coefficients by a factor of 64, using the same approach as Karleskind et al. (2011). Biharmonic horizontal mixing coefficients are $3 \cdot 10^7 m^4/s$ for temperature and salinity and 0 for biogeochemical tracers in the standard case; they are $192 \cdot 10^7 m^4/s$ for all tracers in the viscous case. Horizontal viscosity is $2.7 \cdot 10^8 m^4/s$ in the standard case and $172.8 \cdot 10^8 m^4/s$ in the viscous case. The enhanced viscosity and diffusivity damp but do not eliminate variance at wavelengths below 60 km. The comparison between the two cases allows us to explicitly quantify the impact of the resolved submesoscales in the standard run. Each simulation is run for 3.5 years. The effectiveness of increased viscosity in reducing submesoscale energy has been discussed in Richards et al. (2021). There, the reduced kinetic energy in the viscous case is evident in the steep slope of the horizontal kinetic energy spectra for wavelengths shorter than 100km and the suppression of vertical kinetic energy at wavelengths shorter than 25km. Horizontal and vertical kinetic energy spectra from our simulations are shown in supplement figures S3 and S4.

Area-mean temperature, salinity, and potential density are strongly controlled by the boundary conditions, showing very little difference between the standard and viscous runs under either climate (see seasonal cycles in supplement figures S1 and S2). The mixed layer depth (MLD) is also very similar, with a 215 m maximum in March in the 2000s and a 75 m maximum in March in the 2100s. The only noticeable difference with viscosity consists of the response to an April storm in the 2000s, which remixes the viscous run deeper than the standard, with the mixed layer depth reaching 100m rather than 60m (see figure 1ab, black curves). Increased viscosity does have a direct effect on the velocity, and we consider the root-mean-squared vertical component of velocity representative of the submesoscale activity. In the 2100s, the maximum root-mean-squared vertical components of velocity are about one-third of those in the 2000s. The viscous

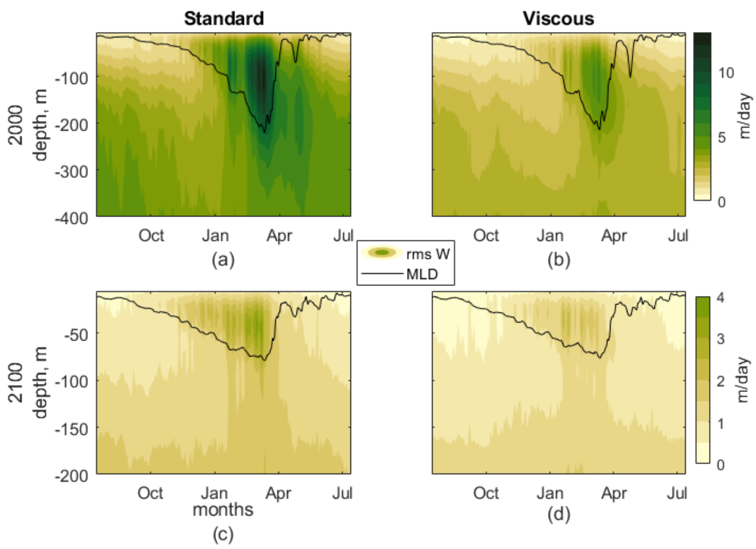


**Figure 1.** Seasonal cycle of root-mean-squared vertical component of velocity, from domain and 36-hour means. Black curves are mixed layer depth, using the same averaging. (a) standard run, 2000s; (b) viscous run, 2000s; (c) standard run, 2100s; (d) viscous run, 2100s.

runs have maximum root-mean-squared vertical component of velocity about 50% of those in the standard runs in both climates.

## 2.2 Biogeochemical model

We developed a simplified biogeochemical model to provide an idealized representation of new production and export in the context of the responses of these biological rates to the physical scenarios described above. This section describes the assumptions used to design the tracers and their mathematical form; G. J. Brett et al. (2021) introduced a nearly identical model to examine global new production. To explicitly represent the supply of inorganic nutrient from depth and new production requires one nutrient tracer (e.g., McGillicuddy Jr et al., 2003); a second tracer can represent the phytoplankton that is created and follow it to depth.

In designing the nutrient tracers, we make two simplifying assumptions. First, we assume that the deep nutrient pool is not dependent on local remineralization, which decouples the nutrient tracer from the phytoplankton tracer. For our domain size and several-year simulation period, the lateral nutrient supply is much stronger than the supply from local remineralization would be. Second, we assume that new production depends on the availability of this nutrient and light alone, not on the water temperature, regenerated nutrient, or on the existing plankton population that may be sustained by recycling of nutrients; this omits processes thought to be important in bloom-type events (e.g., Behrenfeld & Boss, 2014) and precludes exponential growth but keeps the nutrient tracer decoupled from all others.

With these simplifying assumptions, the reactions of the nutrient, $N$, is governed by the following equation:

$$\frac{dN}{dt} = -\mu_0 QL \tag{1}$$

$$Q = (N)/(k_N + N) \tag{2}$$

$$L = 1 - e^{-\alpha I} \tag{3}$$

where $\mu_0$ is the maximum growth rate (0.37 mmol N$m^{-3}$ day), $Q$ is the nutrient limitation (nondimensional), $L$ is the light limitation (nondimensional), $k_N$ is the half-saturation constant for the nutrient (3.2 mmol N$m^{-3}$), and $\alpha$ is the sensitivity for the light limitation (0.035 $m^2W^{-1}$). Light, $I$ (W$m^-2$), decays exponentially with a vertical scale of 10m from the surface value of PAR (photosynthetically active radiation), 0.4 times the incoming short-wave radiation. The values of the parameters controlling production, $k_N$, $\mu_0$, and $\alpha$, are optimized via trial and error so that the light and nutrient limitation functions approximately match those of D. B. Whitt & Jansen (2020), who optimized a similar model to fit the observed climatological seasonal cycle of upper-ocean nitrate averaged over whole subpolar North Atlantic.

Initial and boundary conditions for $N$ are based on a nitrate-potential density ($\sigma_\theta$) relationship derived from monthly gridded 1°climatology in the World Ocean Atlas (Garcia et al., 2013), applied to the physical initial and boundary conditions from the global CESM run. In the current climate, this is a direct application; the mean relationship and its range are shown in figure 2. The integrated effects of physical circulation and production set this $N{-}\sigma_\theta$ relationship, and it is difficult to know how it will change with a warming climate, for all the reasons discussed in the introduction. For the late-century climate, we will primarily discuss results using the same $N{-}\sigma_\theta$ relationship as the early century, which is the simplest choice. Another reasonable choice would be to follow the protocol of the physical variables, by deriving mean anomalies in the nitrate-potential density relationship from the CESM-LE and adding them. These mean anomalies are about as large as half the range of the observed relationship. The anomalies added to the mean WOA relationship are also shown in figure 2.

We aim to explicitly represent the export from the surface to the deep ocean with a second tracer. This export is a combination of plankton and detritus, but should be the same total mass, on average, as the supply of nutrient upward. We do not differentiate between different types of sinking organic matter, and refer to them as a whole as *particles*. In reality export occurs via a wide and variable range of particle sizes and sinking speeds, but here we reduce the complex physics, biology, and chemistry of the export processes to a small set of key parameters that are held constant in each experiment and then varied across experiments in a sensitivity study. We assume that there is a constant sinking rate and a constant remineralization rate. Particles, $P$, have their reactions governed according to the following equation:

$$\frac{dP}{dt} = \mu_0 QL - P/\tau + w_s \frac{\partial P}{\partial z}, \tag{4}$$

where $\tau$ is the timescale of remineralization (days) and $w_s$ $(md^{-1})$ is the vertical sinking rate of particles. There is no flux through the air-sea or sea-land interfaces. The initial and boundary condition for $P$ is $P = 0$. For both $N$ and $P$, advection and mixing are applied by the existing ROMS mechanics for passive tracers.

The two parameters that affect export directly are the sinking and remineralization rates. In equilibrium, with constant production, these would set the vertical scale over which particle concentrations would fall. We call this scale $\delta$,

$$\delta = w_s \tau. \tag{5}$$

Our main case will use parameters $w_s = 5md^{-1}$, $\tau = 50$ days, $\delta = 250$m. We will describe, for the 2000s climate, how varying these parameters impacts export rates and the timing of the peak flux. Varying the parameters also provides insight into how submesoscales might impact the pathways to and corresponding mechanisms of export and remineralization e.g., contributions from the biological sinking pump vs. eddy subduction pump (Boyd et al., 2019; Dever et al., 2021). This will be used to discuss how expected reductions in sinking rates in a warmer climate, due to the increased predominance of

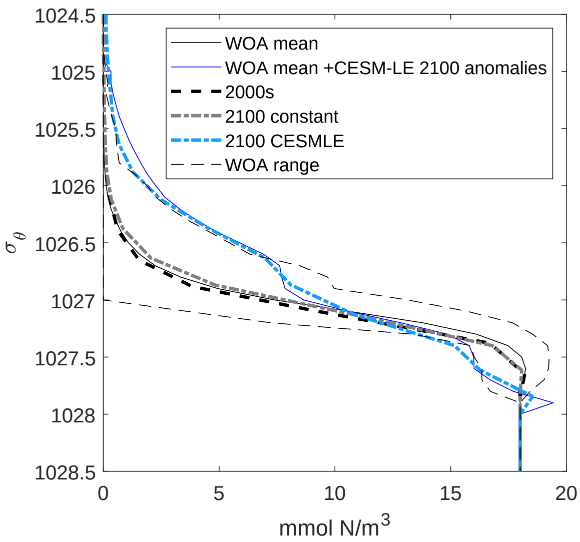


**Figure 2.** The relationship between nutrient concentration ($mmolm^{-3}$) and potential density ($kgm^{-3}$). Solid black line shows the mean observed nitrate-density relationship from the World Ocean Atlas in our domain. The thin dashed black lines show the range of that observed relationship used at the domain boundaries. Thin blue line shows the offset derived from CESM-LE added to the mean observations. Thick dashed lines show the model output's mean $N$ relationship to potential density in our standard runs, which remains similar to the initial conditions.

smaller-celled plankton (Laufkötter et al., 2016), could act as a feedback on our modeled changes in export.

### 2.3 Analysis

Submesoscale fluxes are computed by removing a mesoscale component from snapshots of both the vertical component of the velocity and the relevant concentration (buoyancy, nutrient, particle) to reach a submesoscale component for both and using the product of those components. The mesoscale component is formed using eight applications of a five-point filter in both zonal and meridional directions along a given depth (as done in Capet, Campos, & Paiva, 2008; Richards et al., 2021). An alternate method, removing just the mean and a linear trend across the domain, gives fluxes of the same magnitude and seasonal cycles in all cases examined, but is generally noisier; examples are shown in supplement figures S5, S6.

Seasonal cycles of various fields are formed from 36-hour average fields, which are then averaged over the full domain and subsequently over 3 years, each starting July 16, which excludes the first six months of the runs. Timeseries shown for the full simulation period are formed from snapshots taken every 5 days at noon UTC.

References to seasons define winter as January, February, and March; spring as April, May, and June; summer as July, August, and September; and fall as October, November, and December.

# 3 Results

## 3.1 Production

In this section, we use a single set of biogeochemical parameters and our four physical scenarios to examine the effects of climate change on new production. The four physical scenarios include the standard and viscous cases for year 2000 and year 2100 climates. Our analysis builds on the results of Richards et al. (2021), who showed that submesoscale energy is reduced in a warmer climate, primarily in the winter. In this study, we quantify the impacts these climate-driven changes have on biogeochemical tracers and surface ocean production. This will allow us to describe the potential impact of improved resolution on climate projections of production and export in this region.

By design, the mean nutrient profile set at the boundaries is the same between the standard and viscous runs, such that differences in the seasonal cycles of nutrients (figure 3) are due to local processes and may be interpreted as due to the differing submesoscale activity. These seasonal cycles are qualitatively similar across runs in both climates. In the early century, nutrients are depleted at the surface in the summer and replenished via entrainment when the mixed layers are deep, with maximum surface concentrations in late March. In the warmer climate, nutrient concentrations are reduced in the winter mixed layer and seasonal thermocline by up to 2 mmol $m^{-3}$. These reductions in the nutrient concentration reflect the modified boundary conditions which represent a reduced supply of nutrients by the large-scale circulation. In addition, the nutrient concentration in the warmer climate has a weaker seasonal cycle overall (see figure 3d,e). Just below the mixed layer, nutrient concentrations are slightly higher for the standard run, while the viscous run has higher nutrient concentrations below 120m depth.

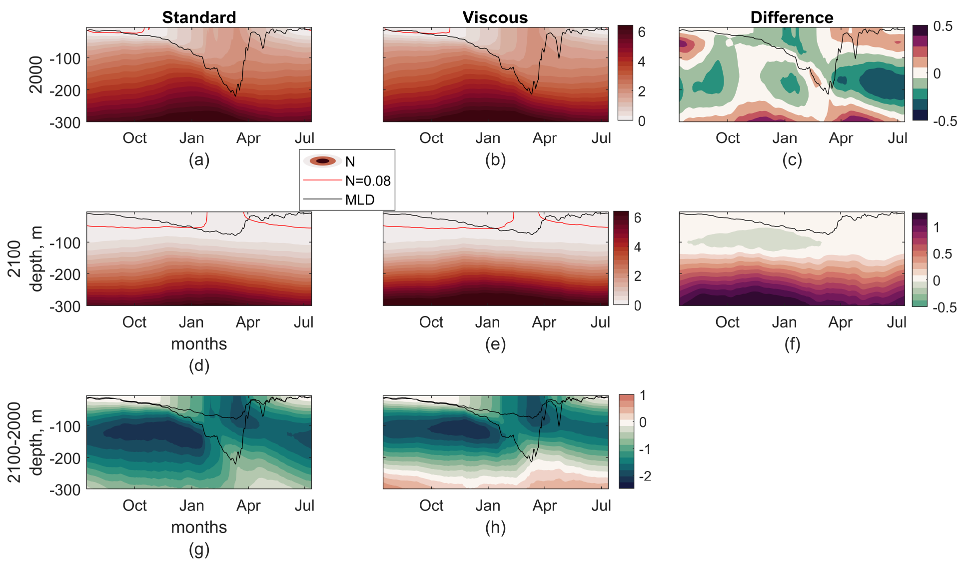


**Figure 3.** New nutrient, $N$, concentration, mmol m$^{-3}$, from domain and 36-hour means, with a 3-year mean to show the seasonal cycle. Black curves are mixed layer depth, using the same averaging. Red curves are $N = 0.08$, which is one-fourth of $k_N$. (a) standard run, 2000s; (b) viscous run, 2000s; (c) difference, viscous-standard, 2000s;(d) standard run, 2100s; (e) viscous run, 2100s; (f) difference, viscous-standard, 2100s; (g) standard runs, difference, 2100s-2000s; (g) viscous runs, difference, 2100s-2000s.

New production rates are also qualitatively similar between the standard and viscous runs (figure4). In the 2000s, the small differences between the standard and viscous runs' new production rates have the same sign and similar spatial pattern as the small differences in their nutrient concentrations. Because the light conditions and production function match, the nutrient differences drive the production differences. In the fall and winter, the standard run has higher nutrient concentrations in the mixed layer, likely related to higher vertical mixing rates (figure 1), with correspondingly higher new production and particle concentration. As the mixed layer shoals in late March and April, the nutrient concentrations in the top 100m become higher in the viscous run, as do the new production rates and the particle concentrations, and these higher values persist through August. The mixing associated with the April storm briefly reduces the differences between the standard and viscous runs in the near-surface values of these fields, indicating that different rates of vertical mixing may drive these small domain-wide differences.

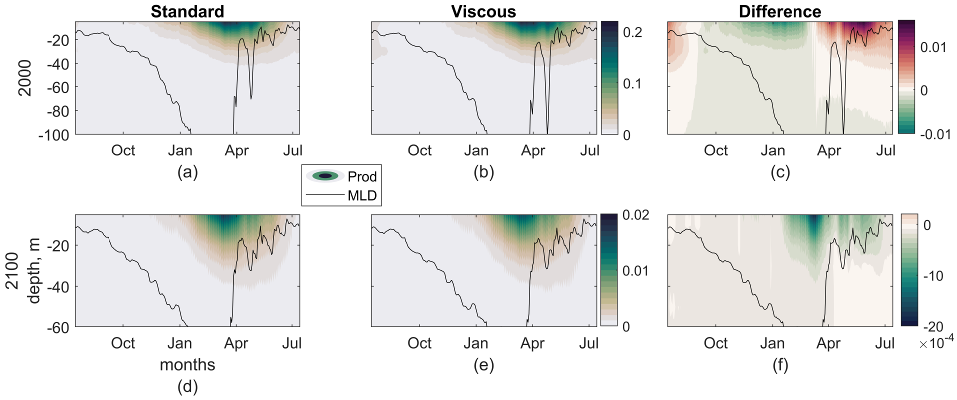


**Figure 4.** New production rate, mmol m$^{-3}$ d$^{-1}$, from domain and 36-hour means, with a 3-year mean to show the seasonal cycle. Black curves are mixed layer depth, using the same averaging. (a) standard run, 2000s; (b) viscous run, 2000s; (c) difference, viscous-standard, 2000s;(d) standard run, 2100s; (e) viscous run, 2100s; (f) difference, viscous-standard, 2100s.

The new production rate in the warmer climate shows a lower peak rate and shortened growing season in comparison to the 2000s (figure 4). The peak rate is about 10% of that in the 2000s, which creates a similarly-reduced peak in phytoplankton concentrations (not shown). As in the 2000s, the domain-mean seasonal cycle of production is very similar for the standard and viscous cases. There is lower production in the viscous run at all times, about 1% on average. The largest differences are about 10% in the top 20m in late March, when production is highest as the mixed layer shoals and surface nutrient concentrations are at their maxima. The shoaling mixed layer may differently impact the nutrient concentration in the standard and viscous runs as different amounts of submesoscale processes like mixed layer instabilities are resolved.

Integrating the new production to 100m depth, the domain-mean rates for the four cases discussed above, as well as the two cases for 2100s with the altered nutrient-potential density boundary condition, shows clearly that the reductions associated with the warmer climate are much larger than the differences between the standard and viscous runs in either climate (figure 5, table 1). The annual peak production is still in March each year in all cases using this measure. The reduced length of the growth season is also clear here for all 2100s runs, with very little growth in December and early January in the warmer climate. The effect of the choice of nutrient boundary conditions is very large. Maintaining the nutrient-density relationship across climates leads to low nutrients in the more-

**Table 1.** Domain and time averaged new production rates integrated over the top 100m.

| Climate | Nutrient boundary conditions | Viscosity | Mean new production, $mmolN/m^2$ |
|---|---|---|---|
| 2000 | WOA | standard | 2.50 |
| 2000 | WOA | 64x viscosity | 2.73 |
| 2100 | WOA | standard | 0.195 |
| 2100 | WOA | 64x viscosity | 0.188 |
| 2100 | CESM LE | standard | 1.37 |
| 2100 | CESM LE | 64x viscosity | 1.32 |

buoyant surface ocean, driving a mean percent reduction in production of 92.7% for the standard run and 93.6% for the viscous run. Adjusting the nutrient-density relationship based on CESM-LE increases the nutrient concentrations such that production is reduced by only about 45% from the current climate. This effect is analogous to different basin-scale and larger changes in nutrient transport with the warming climate. The dominance of this large-scale, remote driver of production over the local effects of resolving more of the submesoscale is consistent with previous results that the area-integrated effects of submesoscales on production are small (≤5% in Karleskind et al., 2011; Levy, Iovino, et al., 2012; Levy & Martin, 2013) and that large-scale circulation can dominate local effects for nutrient concentrations in a global warming scenario (D. B. Whitt & Jansen, 2020).

The percent change in production from the 2000s to 2100s climate with the constant, WOA-based, nutrient-potential density boundary condition, is similar for both the standard and viscous cases, varying between -88% and -96% (figure 5). The differences in the percent reduction of production are small and have some seasonal dependence, with larger reductions for the viscous case in May through July. This seasonal dependency is consistent across boundary conditions (not shown), and is due to higher summer production in the 2000s for the viscous case. The similarity in percent reduction regardless of the inclusion of more-resolved submesoscales suggests that resolving the submesoscale may not be necessary for accurate climate projections.

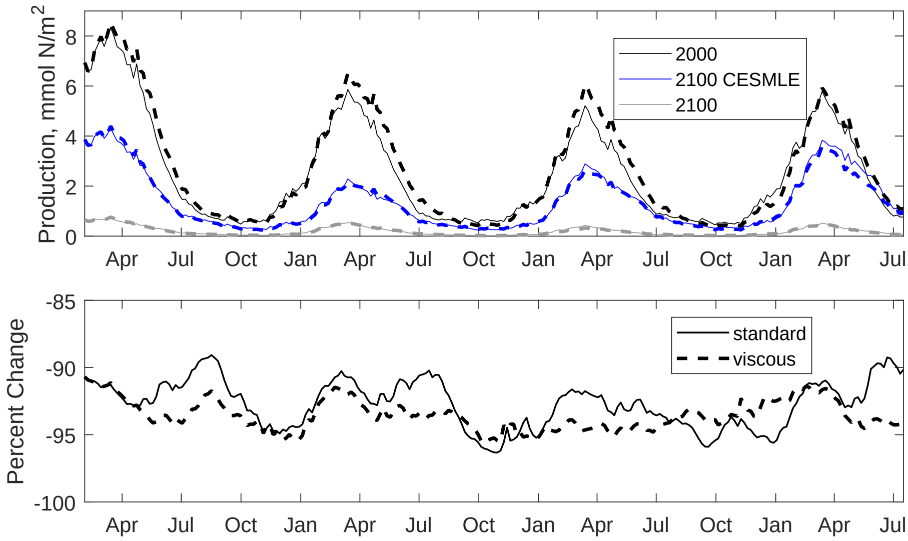


**Figure 5.** Top panel: Snapshots of new production integrated over the top 100m, mmol/m2day, every 5 days; colors indicate which of 3 types of runs is represented: 2000s, 2100s climate with same boundary conditions, and 2100s climate with a nutrient-potential density relationship altered based on the CESM-LE. Dashed lines indicate the viscous runs, solid the standard runs. Bottom panel: percent change from 2000s to 2100s for cases with constant boundary conditions.

## 3.2 Vertical Fluxes

In this section we examine the downward flux of particles, which is composed of both gravitational sinking, $w_sP$ where $w_s$ is constant in space and time, and advective sinking, $wP$ where $w$ is the vertical water velocity. The submesoscale component of advective sinking, $w'P'$, is of particular interest because we know that in the warmer climate the submesoscale kinetic energy is substantially reduced (Richards et al., 2021). Before examining the changes in vertical particle fluxes with a warming climate, where we used constant parameters $w_s$ and $\tau$, we describe the relationship between the components of the flux at 100m depth with varying $w_s$, $\tau$, $\delta$ in our standard run in the 2000s.

### *3.2.1 Sensitivity to parameters*

To understand the relative contributions of gravitational and advective export to the total export flux, and the proportion of the advective export due to submesoscales, we examine the domain-mean export flux at 100m depth in the early-century standard runs for a range of values of $w_s$ and $\tau$. The time-average values from all experiments are shown in figure 6. To isolate the effect of $w_s$, we hold $\tau$ at 50 days and use four values of $w_s$: 1.26, 2.5, 5, and $10md^{-1}$. This produces a range of $\delta$ values from 63 to 500m. To understand how changes in $\tau$ and $w_s$ interact, we also hold $\delta$ at 125m and vary $\tau$ over 6, 25, 50, 100, and 200 days, so that $w_s$ varies from 20.83 to 0.625 $md^{-1}$. In the time-average, total export is dominated by the gravitational component in all cases, and the advective component, due to the vertical component of water velocity, is dominated by its submesoscale component. Increasing $w_s$ increases the gravitational flux and decreases the advective flux, in part because higher gravitational sinking reduces the available particle concentration at this depth. Co-varying $w_s$ and $\tau$ has a larger effect on advective export than on the gravitational component, but these nearly compensate so that the effect on total export is quite small.

Timeseries of the domain-averaged export flux and its components show their variation in magnitude and seasonal cycle as we vary $w_s$ and $\tau$ (figures 7 and 8). The peak flux values for gravitational sinking can reach an order of magnitude larger than those of the advective flux, despite the fact that their average values are more similar. Peak submesoscale advective fluxes are in March and April in all cases, but the gravitational peak varies from April to October, arriving later in the year for slower $w_s$ and longer $\tau$.

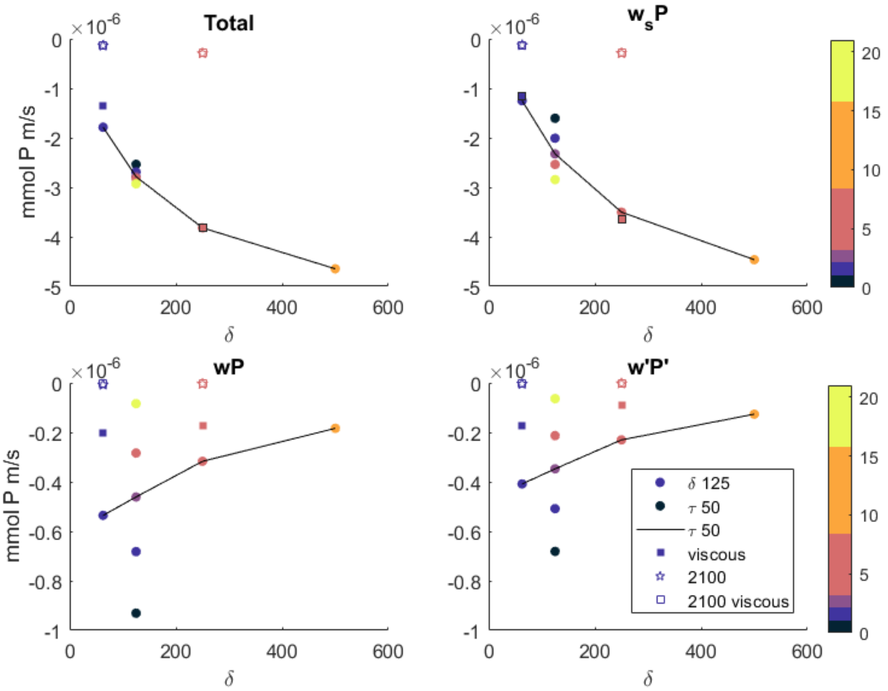


**Figure 6.** Time- and domain-mean vertical flux of plankton at 100m depth; mmol m/s. Top left, total. Top right, only gravitational sinking component. Bottom left, only advective component. Bottom right, submesoscale portion of advective component. In all rows, filled circles are for the 2000 standard run. Colors indicate different values of the gravitational sinking rate, $w_s$; the black line links the points where $\tau = 50d$.

The submesoscale advective component of export is never the dominant component of total export. However, for slow sinking (small $w_s$) and slow remineralizing (long $\tau$), its peak value reaches up to 26% of the peak total export rate. This falls to 4% for our fastest sinking and remineralizing case. The time-average contribution of submesoscale advective flux similarly ranges from 3 to 23% of the total export flux at 100m. Submesoscale advection thus can contribute noticeably to total export, especially when it peaks during the year, but it will be more important for particles that sink slowly and persist over relatively long times.

#### *3.2.2 Climate and viscous effects*

We now examine the vertical particle flux at 100m depth in both viscous and standard runs in both early- and late-century climates (figures 6, 9-10). As for the varied parameters in the 2000s, most of the export in all cases is due to the gravitational sinking, and most of the vertical advection is due to the submesoscale. We present two studies of changes in climate for both standard and viscous runs. One continues our detailed study of $w = 5md^{-1}, \tau = 50d, \delta = 250m$; for comparison we include the 100m vertical particle fluxes of the $w = 1.26md^{-1}, \tau = 50d, \delta = 63m$ case.

For our standard parameters, $\delta = 250m$, the early-century cases show small differences between standard and viscous runs in the total or gravitational export flux. The total export flux is 3% lower for the standard than the viscous case, with a smaller gravitational component partially compensated by a larger advective component (figures 6,9). In the late-century (note the right-hand y-axes in figure 9), the total flux is 3% higher for the standard than the viscous case, with all components slightly higher. These differences in the total and gravitational fluxes between standard and viscous runs are small compared to the reduction in the total flux with a warmer climate of 90.3% for the standard case and 91.2% for the viscous case. These reductions with the warmer climate are similar to the reduction in production of 88-96%, which is clear from the alignment of the fluxes with a ten-fold change in y-axis scale in figure 9. The seasonal cycle shows a larger gravitational flux earlier in the year in the later-century which carries over into the total flux in the first two winters. Results for different boundary conditions in the late-century runs are available in the supplement section S3.

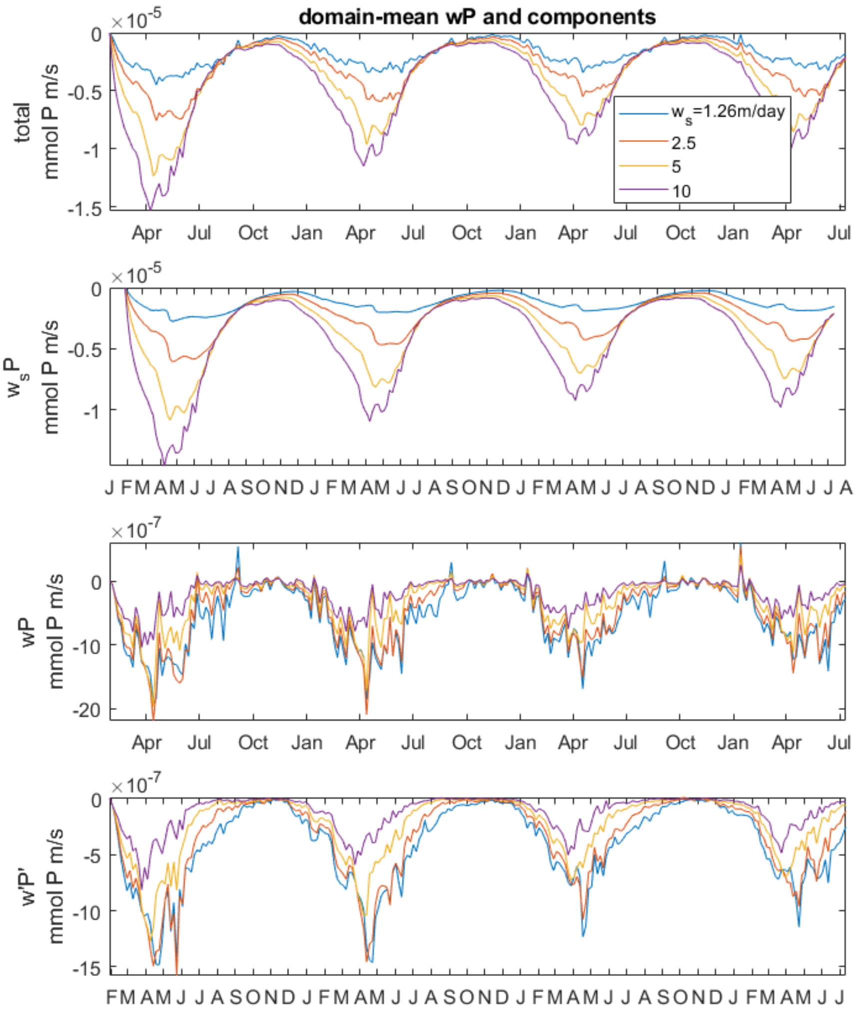


**Figure 7.** Vertical flux of plankton at 100m depth; mmol m/s. Top, total. 2nd row, only explicit sinking component. 3rd row, only advective component. Bottom, submesoscale portion of advective component: for both w and P, a spatially-smoothed field from 8 passes of a 5-point filter is removed to reach the submesoscale component. In all rows, colors indicate 4 different values of the explicit sinking rate. Decay rate, $\tau$, is held constant at 50 days.

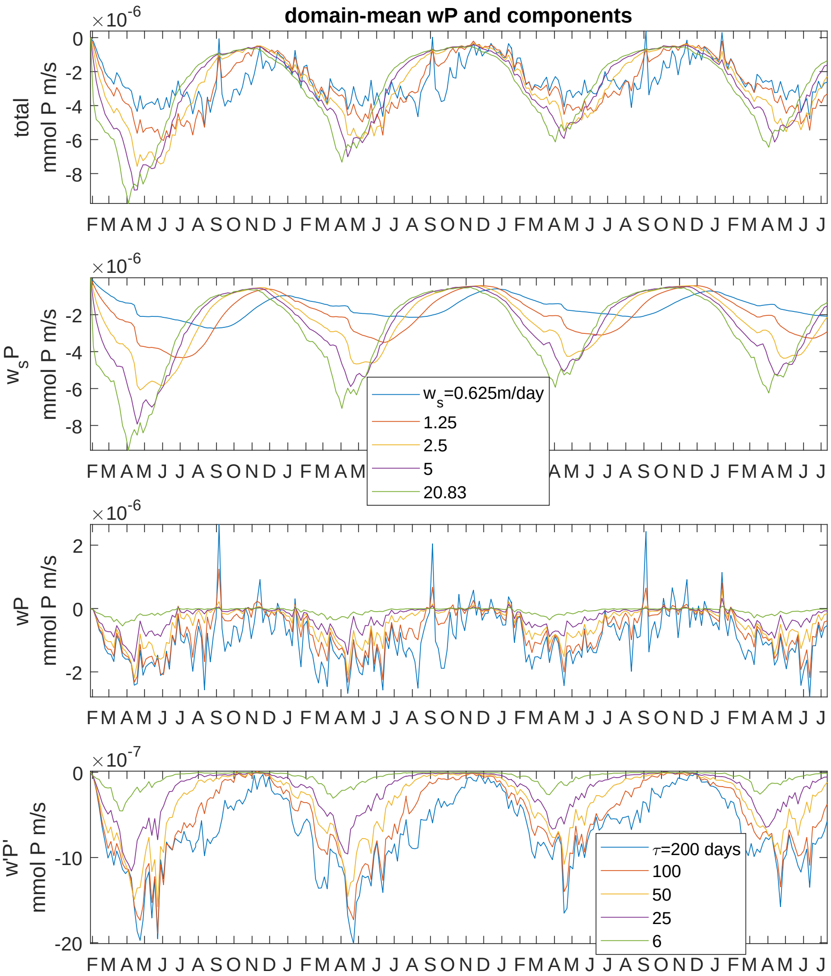


**Figure 8.** Vertical flux of plankton at 100m depth; mmol m/s. Top, total. 2nd row, only gravitational sinking component. 3rd row, only advective component. Bottom, submesoscale portion of advective component: for both w and P, a spatially-smoothed field from 8 passes of a 5-point filter is removed to reach the submesoscale component. In all rows, colors indicate 5 different values of the gravitational sinking rate, $w_s$, and decay rate, $\tau$, varied such that their product is always 125m.

For $\delta = 63m$ (figure 10), in the early-century climate the total export flux is 24% higher for the standard than the viscous case; the gravitational sinking component shows clear differences in the first two winters. In the late-century, the total export flux is 6% smaller for the standard than the viscous case, largely due to different gravitational fluxes in the second winter. The signs of these differences are opposite those of the $\delta = 250m$ case, and the differences are larger. Thus, accurately representing the sinking rate, $w_s$, which drives the gravitational flux, may be very important in correctly projecting carbon export in the future climate. Nonetheless, the export reductions remain similar to the reductions in production: a 92.3% decrease in the standard case and an 89.3% decrease in the viscous case.

The particle advective fluxes show larger effects of both viscosity and climate than the gravitational fluxes. For $\delta = 250m$ the early-century advective flux in the standard case is 60% larger than the viscous, with largest differences in February to April. In the 2100s, the advective fluxes are much smaller, reduced by 97.9% for the standard and 98.5% for the viscous case, and have a similar relationship, with the standard case 69.9% larger. These relationships hold for $\delta = 63m$, with advective fluxes 61-63% smaller in the viscous cases, and 98-99% smaller in the warmer climate.

The submesoscale components have similar relationships between cases as the total particle advective fluxes. For $\delta = 250m$ the mean $w'P'$ is 59.6% larger in the standard case than the viscous in the early-century climate and 50.3% larger in the standard case in the warmer climate. However, there is a clear separation between the peak values for the standard and viscous submesoscale fluxes in the 2000s, which is not apparent in the total advective fluxes: see the April and May values in the bottom row of figure 9. The reductions with warming are 98.8% for the standard case, similar to the 98.6% in the viscous case. However, the peak submesoscale advective fluxes are reduced more than the peak total advective fluxes, by more than 20-fold rather than about 10-fold; note the reduced right-hand y-scales for the warmer climate in figure 9, which are 10x and 20x their respective left-hand y-scales. Again, these patterns hold for $\delta = 63m$ (see figure 10). Thus, while resolving more of the submesoscale results in much larger advective particle fluxes, the result is only a slightly larger decrease for total particle flux with a warmer climate. The advective fluxes are 2-30% of the total flux, which is dominated by the gravitational sinking component and thus the production rate.

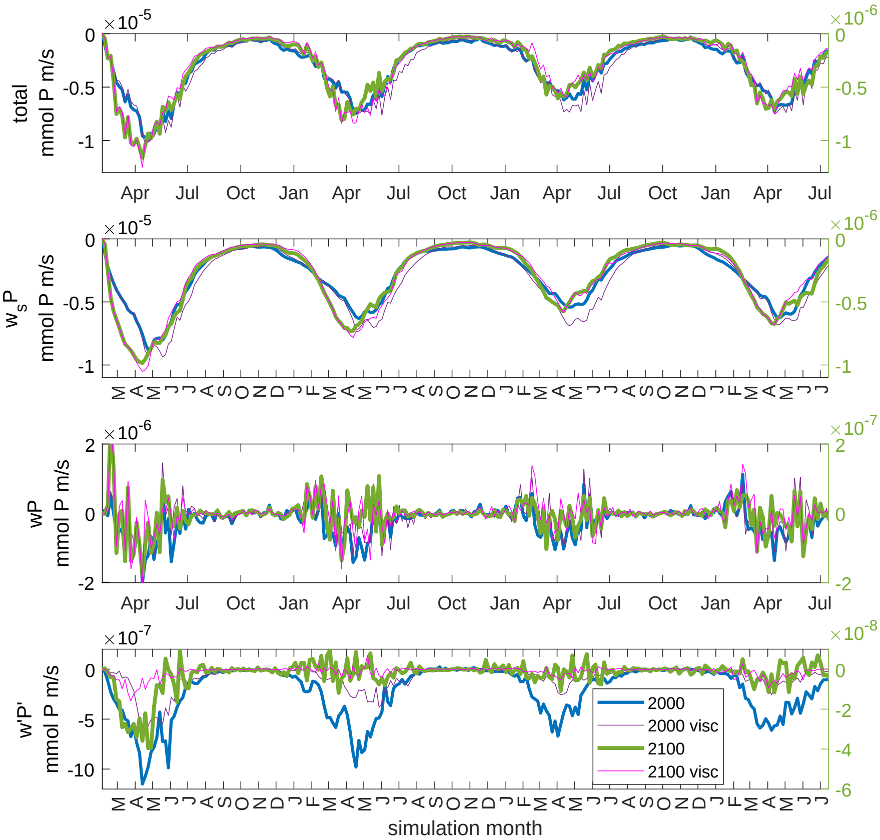


**Figure 9.** Vertical flux of plankton at 100m depth; mmol m/s; $\delta = 250m$. Top, total. 2nd row, only gravitational sinking component. 3rd row, only advective component. Bottom, submesoscale portion of advective component. In all rows, colors indicate which of 4 runs is represented, differentiating standard and viscous runs in both 2000s and 2100s climate. 2000s climate have their y-axis on the left, 2100s on the right. In rows 1-3, the 2100s y-axes are 10x smaller than the 2000s. In row 4, the 2100s y-axis is 20x smaller than the 2000s. All simulations use $w_s = 5md^{-1}$ and $\tau = 50$days. Dark blue lines in this figure correspond to yellow lines in figure 7.

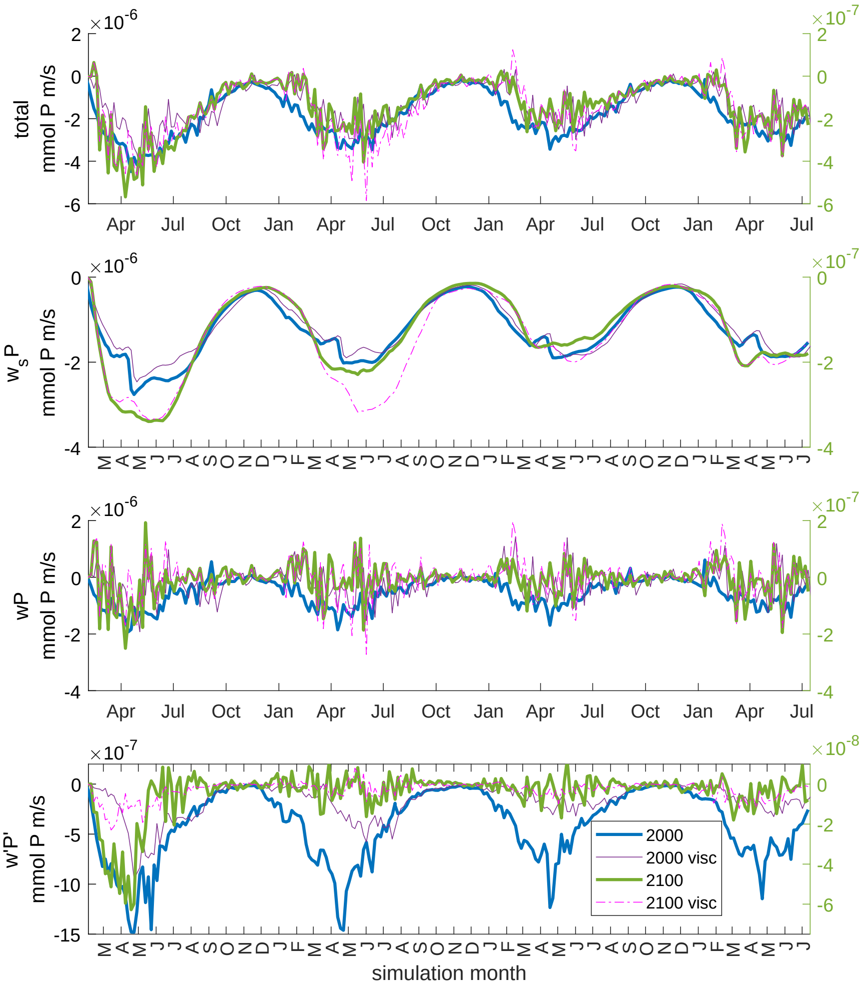


**Figure 10.** Vertical flux of plankton at 100m depth; mmol m/s; $\delta = 63m$. Top, total. 2nd row, only gravitational sinking component. 3rd row, only advective component. Bottom, submesoscale portion of advective component. In all rows, colors indicate which of 4 runs is represented, differentiating standard and viscous runs in both 2000s and 2100s climate. 2000s climate have their y-axis on the left, 2100s on the right. In rows 1-3, the 2100s y-axes are 10x smaller than the 2000s. In row 4, the 2100s y-axis is 20x smaller than the 2000s. All simulations use $w_s = 1.26md^{-1}$ and $\tau = 50$days. Dark blue lines in this figure correspond to blue lines in figure 7.

We now extend our discussion from the particle fluxes at a single depth to the seasonal cycle of submesoscale advective fluxes across depths. For context, we return to the root-mean-squared vertical component of velocity (figure 1), which generally increases from the surface to mid-depth, with lowest values near the surface in the summer and highest values within the mixed layer in the winter in all cases. These high winter vertical velocities are substantially larger in the standard cases than the viscous and in the 2000s climate than the 2100s. The maximum values are $12.9md^{-1}$ for the standard and $5.6md^{-1}$ for the viscous run in the 2000s, and $3.8md^{-1}$ for the standard and $2.3md^{-1}$ for the viscous run in the 2100s. The reduction in the maximum vertical component of velocity with the warmer climate, 70% for the standard and 59% for the viscous case, is larger than the difference between the standard and viscous runs, 56% in the 2000s and 39% in the 2100s, as has been the case across all results. These magnitudes are similar to the submesoscale advective fluxes just discussed.

The submesoscale vertical advection of new phytoplankton is primarily downward at all times (figure 11), with a clear imprint of the magnitude of the vertical component of velocity within the mixed layer. In both climates, the standard case's higher production rates in fall and winter, along with its larger vertical component of velocity within the deep mixed layers, drive stronger winter fluxes than the viscous case. In the 2000s, the largest fluxes are below the shoaling mixed layer in spring, with a strong two-pulse pattern around the April storm in the viscous case and a broader period of stronger downward flux, covering March-June, in the standard case. In the warmer climate, peak submesoscale particle fluxes are 2-5 times weaker and are confined to shallower depths and a shorter period of January to April. The standard case has stronger fluxes when the mixed layer is deepest, while the viscous case has stronger fluxes as the mixed layer shoals. This may be due to stronger submesoscale activity in the standard case when mixed layers are deepest, as indicated by larger vertical water velocities, which increases the advective flux during that period and reduces particle concentrations as the mixed layer shoals.

We contrast these changes in the vertical submesoscale particle fluxes with those of vertical submesoscale buoyancy fluxes (figure 12). The buoyancy fluxes, $w'b'$, are strongest in the winter mixed layer for all cases, and peak values are reduced by half in the warmer climate, which is a smaller change than the peak submesoscale vertical particle fluxes. Notably, peak fluxes are in the winter mixed layer, not below the shoaling spring mixed

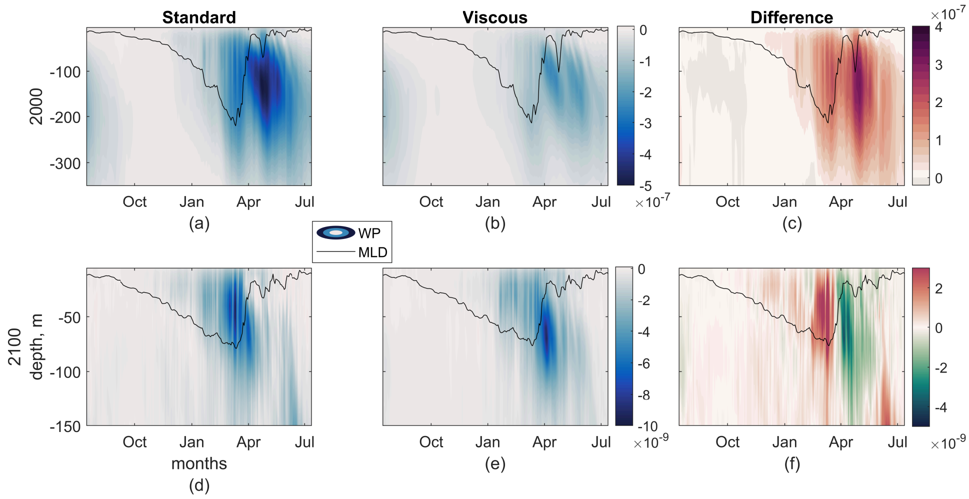


**Figure 11.** Submesoscale portion of advective component of vertical particle flux. For both w and P, a spatially-smoothed field from 8 passes of a 5-point filter is removed at each depth to reach the submesoscale component, from domain and 36-hour means, with a 3-year mean to show the seasonal cycle. Black curves are mixed layer depth, using the same averaging. (a) standard run, 2000s; (b) viscous run, 2000s; (c) difference, viscous-standard, 2000s;(d) standard run, 2100s; (e) viscous run, 2100s; (f) difference, viscous-standard, 2100s.

layer. There are still large fluxes following the April storm, but these do not reach the relative strength that particle fluxes do in that period. Generally, differences in $w'b'$ across viscosities and climates are qualitatively similar to the differences in the magnitudes of the vertical component of the water velocities, suggesting the changes in vertical kinetic energy are the dominant control. In contrast, the submesoscale particle fluxes show much larger changes with a warming climate associated with lower particle concentrations from lower nutrient supply, indicating a possible positive feedback. The different spatial patterns are likely related to the interaction with gravitational sinking, which contributes to the profile of particle concentration being quite different from buoyancy. These differences confirm that we cannot easily extrapolate changes in submesoscale fluxes of biogeochemical tracers from those of physical tracers, supporting continued effort in high-resolution biogeochemical modeling for climate projections.

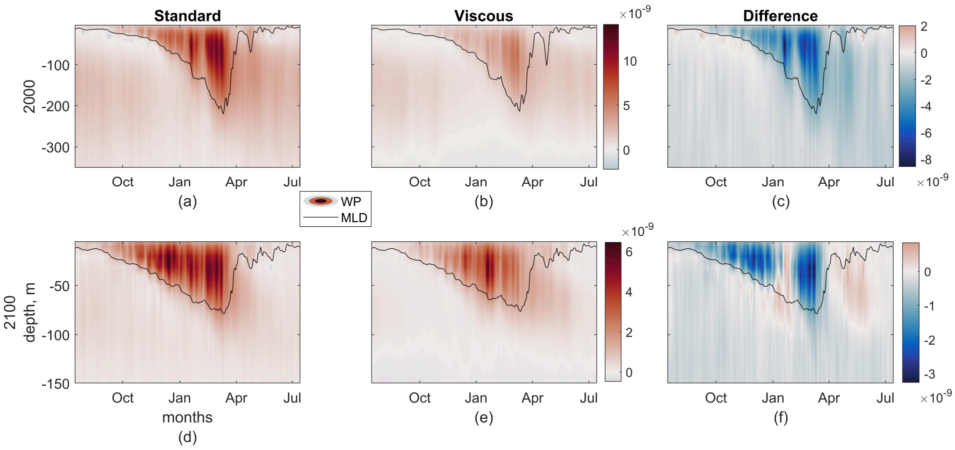


**Figure 12.** Submesoscale portion of vertical component of buoyancy flux. For both w and b, a spatially-smoothed field from 8 passes of a 5-point filter is removed at each depth to reach the submesoscale component, from domain and 36-hour means, with a 3-year mean to show the seasonal cycle. Black curves are mixed layer depth, using the same averaging. (a) standard run, 2000s; (b) viscous run, 2000s; (c) difference, viscous-standard, 2000s;(d) standard run, 2100s; (e) viscous run, 2100s; (f) difference, viscous-standard, 2100s.

## 4 Discussion

In this work we examined the effect of the submesoscale on biogeochemical rates for the Porcupine Abyssal Plain region of the northeast North Atlantic. This is a region where global warming is projected to have a substantial impact, reducing maximum winter MLD (Bopp et al., 2013; Kwiatkowski et al., 2020) and submesoscale activity (Richards et al., 2021). Using a time slice method to create an ocean with climate representative of projections for 2100 under a business-as-usual scenario, increased viscosity to damp the submesoscales in some runs, and an idealized, two-tracer biogeochemistry model, we were able to attribute the role of the local submesoscale in mediating differences in new production and export.

We found that resolving more of the submesoscale has a small impact on annual new production in our small regional domain. In the 2000s climate, nutrient concentration and production are about 10% higher in the fall and winter in the standard run, offset by similarly higher concentrations and rates in the viscous run in spring and summer. Total annual production is larger in the viscous case, consistent with Levy & Martin (2013); Couespel et al. (2021). Levy & Martin (2013) explain this as the negative co-variance of nutrients and phytoplankton concentrations being acted on by submesoscale vertical velocities. In the 2100s climate, the standard run has very slightly higher production throughout the year, with largest differences during the spring restratification. These are likely due to the slight differences in vertical nutrient profiles and the resolved submesoscale motions acting on them as the mixed layer is deepest and then shoaling, similar to the submesoscale buoyancy and particle flux differences. Near-surface nutrient concentrations and new production are substantially reduced in the warmer climate, as set by the changes in the basin-scale state and communicated by the lateral supply from the domain boundaries, consistent with D. B. Whitt & Jansen (2020), with the percent reduction not showing substantial impacts from the inclusion of submesoscales. This suggests that resolution of submesoscale vertical motions may not be necessary for improving local projections of new production.

Recent work by Couespel et al. (2021) using a double-gyre circulation and climate change scenario found similarly small changes in the climate-change response of production for 1/9 and 1/27-degree resolutions. Their production decreases were about 13%, not the 90% that we found, and their 1-degree resolution decreases were only about 26%. They also found that the meridional transport of nutrients was more important than the reduction in vertical supply, with a 27% and 18% decrease, respectively. This dominance of lateral advection is consistent with our results, as is the higher annual production in the 1/9-degree over the 1/27-degree simulations. The differences in magnitude of production decrease with climate may be due to their basin-scale domain, which allowed upscale feedback from the submesoscale to basin circulation.

However, our conclusion of small impacts of submesoscale vertical motions on the response of new production is limited by the scope of this study. First, there are limitations related to the portion of the submesoscale we resolve. With our 4km grid spacing, we are resolving scales of about 12km and larger, which are effective for resolving many submesoscale motions in the winter in the current climate, but not as much in the summer, especially in the warmer climate. The viscous runs limit variability below 60km scales, which while reduced from the standard run, is not a full elimination of submesoscales. Second, our experiment is focused on the role of submesoscales in modifying production locally within the context of a small patch, wherein large-scale vertical gradients in nutrients and stratification were prescribed by a fixed relationship in our boundary conditions. By design, we did not include the feedback of submesoscales to larger scales. This feedback has been shown to shift the large-scale thermocline and nitricline (Levy, Iovino, et al., 2012, , whose domain area is 6x larger). Local changes in mixed layer depths and submesoscale activity have been linked to changes in the basin-scale meridional overturning circulation as well (Fox-Kemper et al., 2011; D. B. Whitt & Jansen, 2020). These shifts would change the lateral nutrient supply, which we found was a dominant control for production under climate change. Finally, this work is specific to its location in the northern North Atlantic. Further work is needed to determine whether our conclusions are applicable more broadly.

In a warmer climate, the export fluxes are largely reduced in proportion to reductions in production, with little contribution from the changes in advection. Using the Boyd et al. (2019) language, the biological gravitational pump is significantly larger than the eddy subduction pump under both climates and dominates the change. The mixed-layer pump, visible in fig. 11, includes the spring detrainment that has no analogue in the buoyancy fluxes and is not well captured in the 100m export flux measurements we used. The biological gravitational pump exports a fairly constant fraction of production under our assumption that $w_s$ and $\tau$ are constant with climate. We have not included the potentially important mechanism of changes in average $w_s$ which would be associated with a projected reduction in mean phytoplankton cell size (Bopp et al., 2005; Fu et al., 2016). Reducing $w_s$ will reduce the export flux and shift the peak flux later in the year. It will also increase the proportion of the export flux due to advection, which in all cases is dominated by its submesoscale component. The submesoscale advective flux is typically 5-25% of the total annual export flux, but shows large effects of warming and the resolution of submesoscale activity. We suggest that high resolution simulations are most important in correctly representing the historical and current state of the ocean and its biogeochemistry, as inaccuracies in the historical and current state cause inaccuracies in the magnitude of projected changes. Submesoscale advective fluxes, while showing clear impact of effective resolution, are a small positive feedback on climate change-related export reductions at the regional scale studied here.

The interplay between sinking and advection in export warrants continued work. In our study, varying relevant parameters and the viscosity showed that increased sinking decreased advective fluxes and vice-versa, such that the sinking flux in the 2000s viscous run is larger than the standard run despite very similar production. Detailed analyses of the interplay of sinking rates and advection are available for the current climate in the work of Dever et al. (2021). The sinking rate, remineralization rate, and magnitudes of vertical velocities together affect the relative export contributions of different sizes of Lagrangian particles. That work was done for a northeast Pacific region, and repeated analysis with a wider range of geographic examples, including larger vertical velocities and faster sinking rates, would assist in climate projections.

In the future, the methods used here could be profitably employed in repeating this study for other regions. Places likely to have different outcomes include the subtropics, eastern upwelling regions, and the Antarctic Circumpolar Current. Until global very high resolution climate projections are possible, there will continue to be a need to estimate the impacts of unresolved processes and improve their parameterization.

## 5 Acknowledgements

This work was funded by the National Science Foundation (NSF) under grants OCE-1658550 and OCE-1658541. This material is based on work supported by the National Center for Atmospheric Research, which is a major facility sponsored by the NSF under Cooperative Agreement No. 1852977. Computing and data storage resources, including the Cheyenne supercomputer (doi:10.5065/D6RX99HX), were provided by the Computational and Information Systems Laboratory (CISL) at NCAR. We thank all the scientists, software engineers, and administrators who contributed to the development of CESM. DBW acknowledges additional support from the National Oceanic and Atmospheric Administration (NA18OAR4310408) and the National Aeronautics and Space Administration (80NSSC19K1116). GJB acknowledges additional support from a Janey grant awarded by Johns Hopkins University Applied Physics Laboratory.

## Open Research

CESM (Lauritzen et al., 2018) is available through
https://www.cesm.ucar.edu/models/cesm2/release_download.html

ROMS (Shchepetkin & McWilliams, 2005) is available through http://www.myroms.org.

The BGC module added to ROMS is in the folder ROMS/Nonlinear/Biology of D. Whitt & Holmes (2021).

Data required for all figures is archived, G. Brett & Whitt (2022).

Codes for making these figures is available, G. Brett (2022). This also requires the package cmocean (Thyng et al., 2016).

## References

Archer, M., Schaeffer, A., Keating, S., Roughan, M., Holmes, R., & Siegelman, L. (2020). Observations of submesoscale variability and frontal subduction within the mesoscale eddy field of the tasman sea. *Journal of Physical Oceanography*, *50*(5), 1509–1529.

Behrenfeld, M. J., & Boss, E. S. (2014). Resurrecting the ecological underpinnings of ocean plankton blooms. *Annual Review of Marine Science*, *6*, 167-194.

Boccaletti, G., Ferrari, R., & Fox-Kemper, B. (2007). Mixed layer instabilities and restratification. *Journal of Physical Oceanography*, *37*(9), 2228–2250.

Bopp, L., Aumont, O., Cadule, P., Alvain, S., & Gehlen, M. (2005). Response of diatoms distribution to global warming and potential implications: A global model study. *Geophysical Research Letters*, *32*(19).

Bopp, L., Resplandy, L., Orr, J. C., Doney, S. C., Dunne, J. P., Gehlen, M., ... others (2013). Multiple stressors of ocean ecosystems in the 21st century: projections with cmip5 models. *Biogeosciences*, *10*, 6225–6245.

Boyd, P. W., Claustre, H., Levy, M., Siegel, D. A., & Weber, T. (2019). Multi-faceted particle pumps drive carbon sequestration in the ocean. *Nature*, *568*(7752), 327–335.

Brett, G. (2022). v1.0 gjayb/submesobioroms: Release with paper submission. doi: 10.5281/zenodo.7315814

Brett, G., & Whitt, D. (2022). Data to reproduce paper: Submesoscale effects on changes to export production under global warming [data set]. doi: 10.5281/zenodo.7314613

Brett, G. J., Whitt, D. B., Long, M. C., Bryan, F., Feloy, K., & Richards, K. J. (2021). Sensitivity of 21st-century projected ocean new production changes to idealized biogeochemical model structure. *Biogeosciences Discussions*, 1–32.

Callies, J., & Ferrari, R. (2018). Note on the rate of restratification in the baroclinic spin-down of fronts. *Journal of Physical Oceanography*(2018).

Callies, J., Flierl, G., Ferrari, R., & Fox-Kemper, B. (2016). The role of mixed-layer instabilities in submesoscale turbulence. *Journal of Fluid Mechanics*, *788*, 5–41.

Capet, X., Campos, E. J., & Paiva, A. M. (2008). Submesoscale activity over the argentinian shelf. *Geophysical Research Letters*, *35(15)*.

Capet, X., McWilliams, J. C., Molemaker, M. J., & Shchepetkin, A. (2008a). Mesoscale to submesoscale transition in the california current system: Flow structure, eddy flux and observational tests. *Journal of Physical Oceanography*, *38*, 29-43.

Capet, X., McWilliams, J. C., Molemaker, M. J., & Shchepetkin, A. F. (2008b). Mesoscale to submesoscale transition in the california current system. part i: Flow structure, eddy flux, and observational tests. *Journal of physical oceanography*, *38*(1), 29–43.

Couespel, D., Lévy, M., & Bopp, L. (2021). Oceanic primary production decline halved in eddy-resolving simulations of global warming. *Biogeosciences*, *18*(14), 4321–4349.

Dever, M., Nicholson, D., Omand, M., & Mahadevan, A. (2021). Size-differentiated export flux in different dynamical regimes in the ocean. *Global Biogeochemical Cycles*, *35*(3), e2020GB006764.

Fox-Kemper, B., Adcroft, A., Böning, C. W., Chassignet, E. P., Curchitser, E., Danabasoglu, G., … others (2019). Challenges and prospects in ocean circulation models. *Frontiers in Marine Science*, *6*, 65. doi: 10.3389/fmars.2019.00065

Fox-Kemper, B., Danabasoglu, G., Ferrari, R., Griffies, S., Hallberg, R., Holland, M., … Samuels, B. (2011). Parameterization of mixed layer eddies. iii: Implementation and impact in global ocean climate simulations. *Ocean Modelling*, *39*(1-2), 61–78. doi: 10.1016/j.ocemod.2010.09.002

Fox-Kemper, B., Ferrari, R., & Hallberg, R. (2008). Parameterization of mixed layer eddies. part i: Theory and diagnosis. *Journal of Physical Oceanography*, *38(6)*, 1145-1165.

Fox-Kemper, B., Hewitt, H. T., Xiao, C., Adalgeirsdottir, G., Drijfhout, S. S., Edwards, T. L., … Yu, Y. (2021). Ocean, cryosphere and sea level change. In V. Masson-Delmotte et al. (Eds.), *Climate change 2021: The physical science basis. contribution of working group i to the sixth assessment report of the intergovernmental panel on climate change* (chap. 9). Cambridge University Press.

Freilich, M. A., & Mahadevan, A. (2019). Decomposition of vertical velocity for nutrient transport in the upper ocean. *Journal of Physical Oceanography*, *49*(6), 1561–1575.

Fu, W., Randerson, J. T., & Moore, J. K. (2016). Climate change impacts on net primary production (npp) and export production (ep) regulated by increasing stratification and phytoplankton community structure in the cmip5 models. *Biogeosciences*.

Garcia, H. E., Locarnini, R. A., Boyer, T. P., Antonov, J. I., Baranova, O. K., Zweng, M. M., … Levitus, S. (2013). World ocean atlas 2013. volume 4, dissolved inorganic nutrients (phosphate, nitrate, silicate).

Glessmer, M. S., Oschlies, A., & Yool, A. (2008). Simulated impact of double-diffusive mixing on physical and biogeochemical upper ocean properties. *Journal of Geophysical Research: Oceans*, *113*(C8).

Gruber, N., Lachkar, Z., Frenzel, H., Marchesiello, P., Münnich, M., McWilliams, J. C., … Plattner, G.-K. (2011). Eddy-induced reduction of biological production in eastern boundary upwelling systems. *Nature geoscience*, *4*(11), 787–792.

Henson, S. A., Laufkötter, C., Leung, S., Giering, S. L., Palevsky, H. I., & Cavan, E. L. (2022). Uncertain response of ocean biological carbon export in a changing world. *Nature Geoscience*, *15*(4), 248–254. doi: 10.1038/s41561-022-00927-0

Karimpour, F., Tandon, A., & Mahadevan, A. (2018). Sustenance of phytoplankton in the subpolar north atlantic during winter. *Journal of Geophysical Research: Oceans*.

Karleskind, P., Lévy, M., & Mémery, L. (2011). Modifications of mode water properties by sub-mesoscales in a bio-physical model of the northeast atlantic. *Ocean Modelling*, *39*(1-2), 47–60.

Kay, J., Deser, C., Phillips, A., Mai, A., Hannay, C., Strand, G., … others (2015). The community earth system model (cesm) large ensemble project: A community resource for studying climate change in the presence of internal climate variability. *Bulletin of the American Meteorological Society*, *96*(8), 1333–1349.

Klein, P., & Lapeyre, G. (2009). The oceanic vertical pump induced by mesoscale and submesoscale turbulence. *Annual review of marine science*, *1*, 351–375.

Kwiatkowski, L., Torres, O., Bopp, L., Aumont, O., Chamberlain, M., Christian, J. R., … others (2020). Twenty-first century ocean warming, acidification, deoxygenation, and upper-ocean nutrient and primary production decline from cmip6 model projections. *Biogeosciences*, *17*(13), 3439–3470. doi:

10.5194/bg-17-3439-2020

Lapeyre, G., & Klein, P. (2006). Dynamics of the upper oceanic layers in terms of surface quasigeostrophy theory. *Journal of physical oceanography*, *36*(2), 165–176.

Large, W. G., & Yeager, S. G. (2004). *Diurnal to decadal global forcing for ocean and sea-ice models: The data sets and flux climatologies* (Vols. TechnicalReport TN-460+STR).

Lathuiliere, C., Levy, M., & Echevin, V. (2011). Impact of eddy-driven vertical fluxes on phytoplankton abundance in the euphotic layer. *Journal of plankton research*, *33*(5), 827–831.

Laufkötter, C., Vogt, M., Gruber, N., Aumont, O., Bopp, L., Doney, S. C., ... others (2016). Projected decreases in future marine export production: the role of the carbon flux through the upper ocean ecosystem. *Biogeosciences*, *13*, 4023–4047.

Lauritzen, P. H., Nair, R. D., Herrington, A., Callaghan, P., Goldhaber, S., Dennis, J., ... Tribbia, J. J. (2018). Ncar release of cam-se in cesm2. 0: A reformulation of the spectral element dynamical core in dry-mass vertical coordinates with comprehensive treatment of condensates and energy. *Journal of Advances in Modeling Earth Systems*, *10*(7), 1537–1570.

Levy, M., Ferrari, R., Franks, P. J., Martin, A. P., & Riviere, P. (2012). Bringing physics to life at the submesoscale. *Geophysical Research Letters*, *39(14)*.

Lévy, M., Franks, P. J., & Smith, K. S. (2018). The role of submesoscale currents in structuring marine ecosystems. *Nature communications*, *9*(1), 1–16.

Levy, M., Iovino, D., Resplandy, L., Klein, P., Madec, G., Treguier, A.-M., ... Takahashi, K. (2012). Large-scale impacts of submesoscale dynamics on phytoplankton: Local and remote effects. *Ocean Modelling*, *43*, 77-93.

Lévy, M., Klein, P., & Treguier, A.-M. (2001). Impact of sub-mesoscale physics on production and subduction of phytoplankton in an oligotrophic regime. *Journal of marine research*, *59*(4), 535–565.

Levy, M., & Martin, A. P. (2013). The influence of mesoscale and submesoscale heterogeneity on ocean biogeochemical reactions. *Global Biogeochemical Cycles*, *27(4)*, 1139-1150.

Löptien, U., & Dietze, H. (2019). Reciprocal bias compensation and ensuing uncertainties in model-based climate projections: pelagic biogeochemistry versus ocean mixing. *Biogeosciences (BG)*, *16*(9), 1865–1881.

Mahadevan, A. (2016). The impact of submesoscale physics on primary productivity of plankton. *Annual review of marine science*, *8*, 161–184.

Mahadevan, A., & Tandon, A. (2006). An analysis of mechanisms for submesoscale vertical motion at ocean fronts. *Ocean Modelling*, *14*(3-4), 241–256.

McGillicuddy Jr, D., Anderson, L., Doney, S., & Maltrud, M. (2003). Eddy-driven sources and sinks of nutrients in the upper ocean: Results from a 0.1 resolution model of the north atlantic. *Global Biogeochemical Cycles*, *17*(2).

McWilliams, J. C. (2016). Submesoscale currents in the ocean. *Proceedings of the Royal Society A: Mathematical, Physical and Engineering Sciences*, *472*(2189), 20160117.

Mensa, J. A., Garraffo, Z., Griffa, A., Özgökmen, T. M., Haza, A., & Veneziani, M. (2013). Seasonality of the submesoscale dynamics in the gulf stream region. *Ocean Dynamics*, *63*(8), 923–941.

Olita, A., Capet, A., Claret, M., Mahadevan, A., Poulain, P. M., Ribotti, A., ... Pascual, A. (2017). Frontal dynamics boost primary production in the summer stratified mediterranean sea. *Ocean Dynamics*, *67*(6), 767–782.

Omand, M. M., D'Asaro, E. A., Lee, C. M., Perry, M. J., Briggs, N., Cetinić, I., & Mahadevan, A. (2015). Eddy-driven subduction exports particulate organic carbon from the spring bloom. *Science*, *348*(6231), 222–225.

Ramachandran, S., Tandon, A., & Mahadevan, A. (2014). Enhancement in vertical fluxes at a front by mesoscale-submesoscale coupling. *Journal of Geophysical Research: Oceans*, *119*(12), 8495–8511.

Resplandy, L., Lévy, M., & McGillicuddy Jr, D. J. (2019). Effects of eddy-driven subduction on ocean biological carbon pump. *Global Biogeochemical Cycles*, *33*(8), 1071–1084.

Richards, K. J., Whitt, D. B., Brett, G. J., Bryan, F. O., Feloy, K., & Long, M. C. (2021). The impact of climate change on ocean submesoscale activity. *Journal of Geophysical Research: Oceans*, *126*(5), e2020JC016750.

Roullet, G., Mcwilliams, J. C., Capet, X., & Molemaker, M. J. (2012). Properties of steady geostrophic turbulence with isopycnal outcropping. *Journal of physical oceanography*, *42*(1), 18–38.

Ruiz, S., Claret, M., Pascual, A., Olita, A., Troupin, C., Capet, A., ... others (2019). Effects of oceanic mesoscale and submesoscale frontal processes on the vertical transport of phytoplankton. *Journal of Geophysical Research: Oceans*, *124*(8), 5999–6014.

Sathyendranath, S., Ji, R., & Browman, H. I. (2015). Revisiting sverdrup's critical depth hypothesis. *ICES Journal of Marine Science*, *72*(6), 1892–1896.

Séférian, R., Berthet, S., Yool, A., Palmieri, J., Bopp, L., Tagliabue, A., ... others (2020). Tracking improvement in simulated marine biogeochemistry between cmip5 and cmip6. *Current Climate Change Reports*, *6*(3), 95–119. doi: 10.1007/s40641-020-00160-0

Shchepetkin, A. F., & McWilliams, J. C. (2005). The regional oceanic modeling system (ROMS): a split-explicit, free-surface, topography-following-coordinate oceanic model. *Ocean modelling*, *9*(4), 347–404.

Smith, K. M., Hamlington, P. E., & Fox-Kemper, B. (2016). Effects of submesoscale turbulence on ocean tracers. *Journal of Geophysical Research: Oceans*, *121*(1), 908–933.

Su, Z., Wang, J., Klein, P., Thompson, A. F., & Menemenlis, D. (2018). Ocean submesoscales as a key component of the global heat budget. *Nature communications*, *9*(1), 1–8.

Sverdrup, H. (1953). On conditions for the vernal blooming of phytoplankton. *J. Cons. Int. Explor. Mer*, *18*(3), 287–295.

Thomas, L. N., Tandon, A., & Mahadevan, A. (2008). Submesoscale processes and dynamics. *Ocean modeling in an Eddying Regime*, *177*, 17–38.

Thyng, K., Greene, C., Hetland, R., Zimmerle, H., & DiMarco, S. (2016). True colors of oceanography: Guidelines for effective and accurate colormap selection. *Oceanography*, *29*(3), 9–13. doi: 10.5670/oceanog.2016.66

Uchida, T., Balwada, D., Abernathey, R., McKinley, G., Smith, S., & Lévy, M. (2019). The contribution of submesoscale over mesoscale eddy iron transport in the open southern ocean. *Journal of Advances in Modeling Earth Systems*, *11*(12), 3934–3958.

Uchida, T., Balwada, D., Abernathey, R. P., McKinley, G. A., Smith, S. K., & Lévy, M. (2020). Vertical eddy iron fluxes support primary production in the open southern ocean. *Nature communications*, *11*(1), 1–8.

Whitt, D., & Holmes, R. (2021). Les and roms software as modified for ncar prefield modelling studies in support of tpos.

doi: 10.5281/zenodo.5716181

Whitt, D. B., & Jansen, M. F. (2020). Slower nutrient stream suppresses subarctic atlantic ocean biological productivity in global warming. *Proceedings of the National Academy of Sciences*, *117*(27), 15504–15510.

Second Supplement to:

Submesoscale effects on changes to export production under global warming

Genevieve Jay Brett[1,2], Daniel B Whitt[3,4], Matthew C Long[4], Frank O. Bryan[4], Kate Feloy[2], Kelvin J. Richards[2]

[1]Johns Hopkins University Applied Physics Laboratory 11100 Johns Hopkins Road, Laurel, MD 20723

[2]University of Hawai'i Manoa 1680 East West Road, Honolulu HI 96822

[3]Ames Research Center, National Aeronautics and Space Administration, Moffett Field, CA

[4]Climate and Global Dynamics Laboratory, National Center for Atmospheric Research, Boulder, CO,

This supplement details the code and data associated with the figures in the paper. The citations of and links to the archived code and data is in the Open Research section of the main paper.

The cmocean package is needed as well, available from https://github.com/chadagreene/cmocean

| Figure number and short description | Code | Data<br>* is a wildcard. Typically this represents the letters a through g or h, or a set of run indicators like _; 64visc_; 2100_v3_; 2100_v3_64visc. |
|---|---|---|
| 1 rms w | plotrmsw.m<br>make_seasonal_fields.m | nprod_10_4km_bipit_del250_means.mat,<br>nprod_10_4km_bipit_del250_64visc_means.mat,<br>nprod_10_4km_bipit_del250_2100_v3_64visc_means.mat,<br>nprod_10_4km_bipit_del250_2100_v3_means.mat,<br>ts_10_4km_bipit_del250_64visc_means.mat,<br>ts_10_4km_bipit_del250_2100_v3_64visc_means.mat,<br>ts_10_4km_bipit_del250_2100_v3_means.mat,<br>ts_10_4km_bipit_del250_means.mat |
| 2 N-density BC | nitratepdenchoices.m | WOA_nsfsubmeso_no3-pden_fit_31_aug_2020.mat,<br>CESMLE_NO3_pden_osmosis.mat, sigmanutriOsmosis2.mat,<br>npden_10_4km_bipit_del250_2100_v3_(a-h)_np.mat,<br>npden_10_4km_bipit_del250_(a-h)_np.mat,<br>npden_10_4km_bipit_del250_2100_v2_(a-h)_np.mat,<br>npden_10_4km_bipit_del250_2100_(a-h)_np.mat |
| 3,4<br>N,<br>production | plotbioset.m<br>make_seasonal_fields.m | ts_10_4km_bipit_del250_*_means.mat,<br>nprod_10_4km_bipit_del250_*_means.mat,<br>pset_10_4km_bipit_del250_*_means.mat |
| 5 integrated production | productionsetPub.m | nprod_10_4km_bipit_del250_*_his.mat |

| | | |
|---|---|---|
| 6 mean vertical fluxes | plotmean100mFlux.m | exportfluxmeansV2.mat |
| 7,8 100m fluxes, varied ws or covaried ws and tau | plotFlux100mVariedParameters.m | wP2000variedws.mat<br>wP2000variedtau.mat |
| 9,10 100m fluxes | plot100mWPclimatechangePub.m | pset_10_4km_bipit_*_his.mat |
| 11, 12 w'P' and w'b' | filtermethodcompare.m<br>make_seasonal_fields.m | ts_10_4km_bipit_del250_*_means.mat,<br>nprod_10_4km_bipit_del250_2100_v3_means.mat,<br>wpwb_10_4km_bipit_del250_*_np.mat |
| S1 physical fields 2000 | plotphysics2000.m | ts_10_4km_bipit_del250_64visc_means.mat,<br>ts_10_4km_bipit_del250_means.mat,<br>nprod_10_4km_bipit_del250_64visc_means.mat,<br>nprod_10_4km_bipit_del250_means.mat |
| S2 physical fields 2100 | plotphysics2100.m | nprod_10_4km_bipit_del250_2100_v3_64visc_means.mat,<br>ts_10_4km_bipit_del250_2100_v3_64visc_means.mat,<br>ts_10_4km_bipit_del250_2100_v3_means.mat,<br>nprod_10_4km_bipit_del250_2100_v3_means.mat |
| S3 KEh spectra | plot_spectra_depth_slice.m | spectra_10_4km_bipit_del250*.mat |
| S4 KEv spectra | plot_seasonal_spectra.m<br>make_seasonal_spectra.m | spectra_10_4km_bipit_del250*.mat |
| S5, S6 w'P' and w'b', different method | filtermethodcompare.m<br>make_seasonal_fields.m | ts_10_4km_bipit_del250_*_means.mat,<br>nprod_10_4km_bipit_del250_2100_v3_means.mat,<br>wpwb_10_4km_bipit_del250_*_np.mat |
| S7 100m fluxes, different boundary conditions | plot100mWPclimatechangePub.m | pset_10_4km_bipit_del250_2100_(a-h)_his.mat<br>pset_10_4km_bipit_del250_2100_64visc_(a-h)_his.mat<br>pset_10_4km_bipit_del250_(a-h)_his.mat<br>pset_10_4km_bipit_del250_64visc_(a-h)_his.mat |

# Supplement to: Submesoscale effects on changes to export production under global warming

**Genevieve Jay Brett[1,2], Daniel B Whitt[3,4], Matthew C Long[4], Frank O. Bryan[4], Kate Feloy[2], Kelvin J. Richards[2]**

[1]Johns Hopkins University Applied Physics Laboratory 11100 Johns Hopkins Road, Laurel, MD 20723, USA

[2]University of Hawai'i Manoa 1680 East West Road, Honolulu HI 96822, USA

[3]Ames Research Center, National Aeronautics and Space Administration, Moffett Field, CA, USA

[4]Climate and Global Dynamics Laboratory, National Center for Atmospheric Research, Boulder, CO, USA

## S1 Physical Model

In this section we provide more detail on the physical model setup and the seasonal cycle of mixed layer depth, temperature, salinity, and squared vertical velocities. For further discussion of the physics, see Richards et al. (2021), which uses nearly-identical simulations.

We use the Regional Ocean Modeling System (ROMS) with a 4km grid to model the Porcupine Abyssal Plain region in the North Atlantic, specifically 41-51°N and 11-27°W. This regional model is in a one-way-nested configuration within a Community Earth System Model (CESM) version 2.0 global model in an "ocean-sea-ice" configuration at a nominal 0.1°forced by atmospheric fields derived from reanalysis representative of a statistically normal annual cycle, i.e. a normal year (Large & Yeager, 2004). To develop a process-oriented means of examining the response of new production and vertical export fluxes to idealized changes in climate, we utilize the "time slice" approach for our global model, as described in Richards et al. (2021) and Brett et al. (2021). Thus, the global model's initial conditions and both models' surface forcing are set to simulate a period representative of either early- or late-century climate conditions, with the adjust-

Corresponding author: Jay Brett, `Jay.Brett@jhuapl.edu`

ments for late-century conditions set by anomalies computed from the fully-coupled CESM1 Large Ensemble (CESM-LE; Kay et al., 2015).

Richards et al. (2021) provide details of the ROMS setup for a 1.25km and 4km resolution grid nested within the same global model runs. The regional model is initialized with February first conditions and run for 4 years. Here we use only the 4km grid with 90 vertical levels, as we saw very small differences between 1.25km and 4km output. To suppress a portion of the submesoscale in what we call the *viscous* runs, as opposed to *standard* runs, we increase the viscosity and diffusivity via increasing the hyperdiffusivity and hyperviscosity coefficients by a factor of 64, which damps but does not eliminate wavelengths below 60km. The comparison between the two cases will allow us to explicitly quantify the impact of the resolved submesoscales in the standard run. Each simulation is run for 3.5 years.

In the 2000s climate, the mixed layer shows a seasonal cycle with its maximum in March near 215m depth, followed by spring shallowing that is interrupted by a noticeable but short storm-induced remixing at the end of April. This cycle is shown in figureS1 as the mean over the domain and three model years, from 6 months after initialization onward. The mixed layer is shallow throughout the summer, with fall mixing noticeable starting in October. The main point of difference between the standard and viscous runs is associated with the April storm, which remixes the viscous run deeper than the standard, with the mixed layer depth reaching 100m rather than 60m.

The increased viscosity has very little impact on area-mean temperature, salinity, and potential density fields throughout the year (figure S1), with temperature differences within 0.5°C, salinity differences within 0.1psu, and densities within 0.05kg/m$^3$. However, the viscous run has slightly cooler, fresher, denser water just below the mixed layer depth in the summer and fall, with slightly cooler, fresher, less dense water within the mixed layer in the fall to winter. The different signs of the density differences are due to asymmetries between temperature and salinity differences during the two time periods. The mean squared vertical components of velocity show the largest effects of increased viscosity, with winter maximum values being about 60% lower in the viscous run. As these velocities are directly impacted by viscosity, this is to be expected.

In the warmer climate, the mixed layer depth has a shallower March maximum near 75m (figureS2 shows the domain and 3-year mean seasonal cycle, from 6 months after

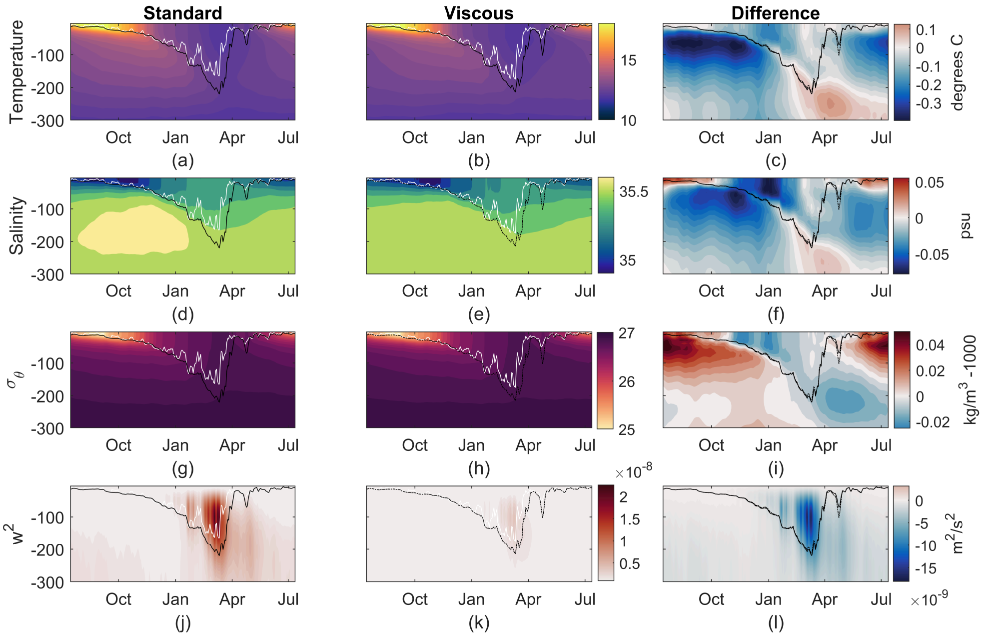


Figure S1: Domain and 3-year mean of temperature (a,b), salinity (d,e), potential density (g,h), and squared vertical component of velocity (j,k) for the 2000s climate. Left column is the standard run (a,d,g,j), middle the high-viscosity run (b,e,h,k), and right the difference, viscous-standard (c,f,i,l). White curves are the boundary layer depth, black curves the mixed layer depth. In the rightmost column, the standard run's mixed layer depth curve is solid while the viscous run's is dashed.

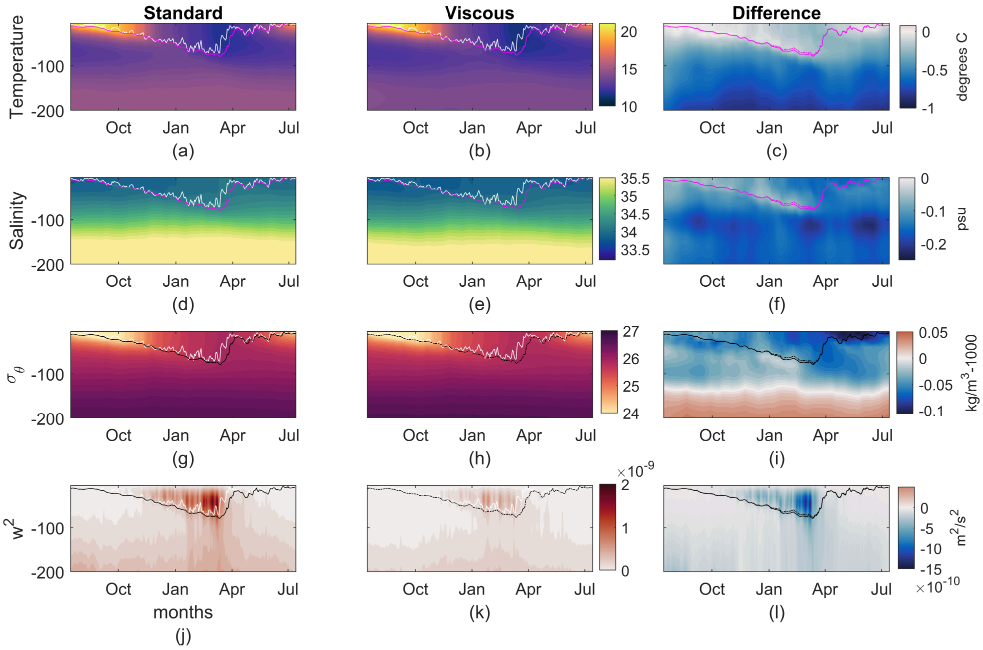


Figure S2: Domain and 3-year mean of temperature (a,b), salinity (d,e), potential density (g,h), and squared vertical component of velocity (j,k) for the 2100s climate. Left column is the standard run (a,d,g,j), middle the high-viscosity run (b,e,h,k), and right the difference, viscous-standard (c,f,i,l). White curves are the boundary layer depth, black and magenta curves the mixed layer depth. In the rightmost column, the standard run's mixed layer depth curve is solid while the viscous run's is dashed.

initialization onward). There is no qualitative difference between the standard and viscous mixed layer depths, and the April storm's effects are much less noticeable. The surface water is warmer, fresher, and less dense than in the 2000s climate, as imposed by the initial and boundary conditions. The viscous runs are cooler, fresher, and less dense than the standard runs throughout the top 150m, which includes the deepest mixed layer depths. As in the 2000s climate, these differences are small. In contrast, the differences in mean squared vertical components of velocity is again large. The standard run in 2100s has maximum $w^2$ about 10% of those in the 2000s standard run. The viscous run in 2100s has maximum $w^2$ about 40% of those in the standard run, the same ratio as in the 2000s runs.

To demonstrate the specific variability reduced in the viscous run compared to the standard run, we show spectra of horizontal and vertical kinetic energy. These spectra focus on the winter mixed layer, when there is the most submesoscale activity. In the 2000s, spectra are at 100m, within the winter mixed layer, and in the 2100s, spectra are at 50m to remain within that winter mixed layer. Spectra are from the snapshots every 5 days. The horizontal kinetic energy spectra, figure S3, do not have a strong seasonal cycle. Maximum horizontal kinetic energy is at wavelengths near 150-210km in all runs. The viscous run has largely reduced kinetic energy below about 60km (-4.8 on the plot y-axes, the log of cycles per meter). Vertical kinetic energy spectra have a strong seasonal cycle, as shown for the vertical velocity in the main text, and so are averaged over the years of the run to show the average seasonal cycle, figure S4. The maximum vertical kinetic energy in the winter is near 19km wavelengths in the standard run and 33km in the viscous run in the 2000s, and 22km in the standard run and 39km in the viscous run in the 2100s. That is to say the vertical kinetic energy is largest near wavelength of 5 grid points in the standard run and 9 grid points in the viscous run. The ratio between the most energetic winter wavelengths is approximately 1.75 (viscous:standard), and there is also a reduction of the maximum energy at those wavelengths by about a factor of 2.

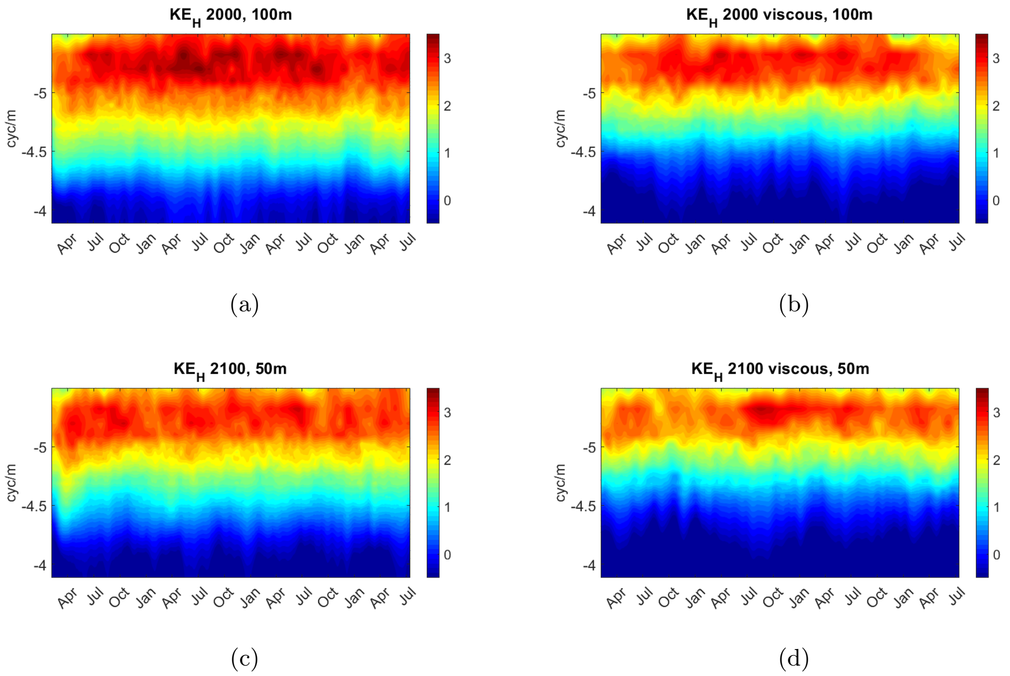


Figure S3: Spectra of the horizontal kinetic energy. Colors are the log (base 10) of the energy, and the y-axes are the log (base 10) of the wavelengths in cycles per meter. (a,b) 2000s, 100m depth. (c,d) 2100s, 50m depth. (a,c) standard runs. (b,d) viscous runs.

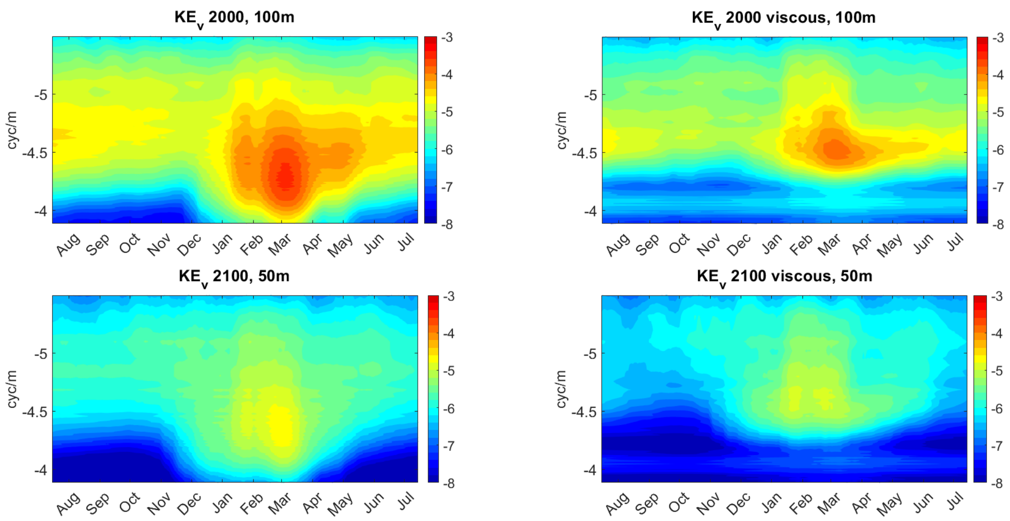


Figure S4: Spectra of the vertical kinetic energy, averaged over the model run years to show the average seasonal cycle. Colors are the log (base 10) of the energy, and the y-axes are the log (base 10) of the wavelengths in cycles per meter. (a,b) 2000s, 100m depth. (c,d) 2100s, 50m depth. (a,c) standard runs. (b,d) viscous runs.

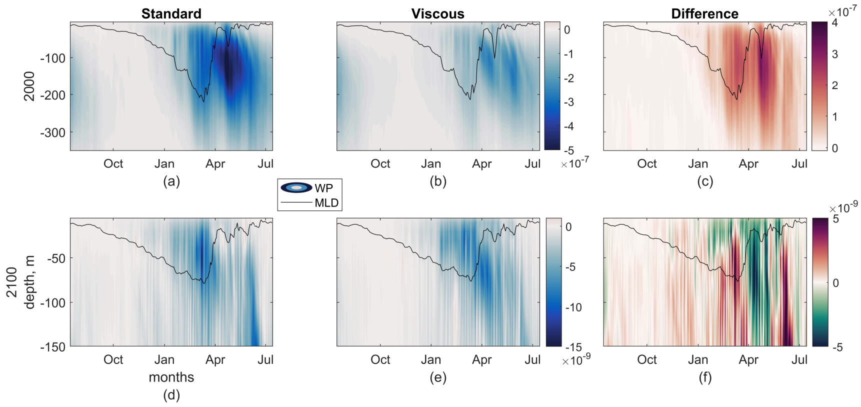


Figure S5: Submesoscale vertical advective particle fluxes from 36hr-mean w and P with spatial mean and linear trends removed. Compare with figure 9 in the main text.

## S2 Submesoscale Analysis

Submesoscale fluxes in the main text are found by removing a mesoscale component from both the vertical component of the velocity and the relevant concentration (buoyancy, nutrient, particle) to reach a submesoscale component for both and using the product of those components. Here we show that the results qualitatively match an alternate method, removing just the mean and a linear trend across the domain from each component. Submesoscale particle fluxes are shown in figure S5 (compare to figure 11) and submesoscale buoyancy fluxes are shown in figure S6 (compare to figure 12).

## S3 Alternate Boundary Condition Flux Results

While in the main text we have focused on the results using the constant WOA-based nutrient-density relationship at the boundaries, here we include results on the export flux with the altered 2100s boundary condition, constructed using the CESM-LE nutrient-density relationship anomalies. Recall that figure 5 in the main text shows the production rate, and that the magnitudes of the vertical component of velocity will be the same as discussed in the main text.

The early-century cases shown here are the same as in figure 8 of the main text. In the late-century cases, the total flux is 3.6% larger in the viscous than the standard case, mainly due to a 3.5% larger gravitational component. These differences in the total and gravitational fluxes between standard and viscous runs are small compared to

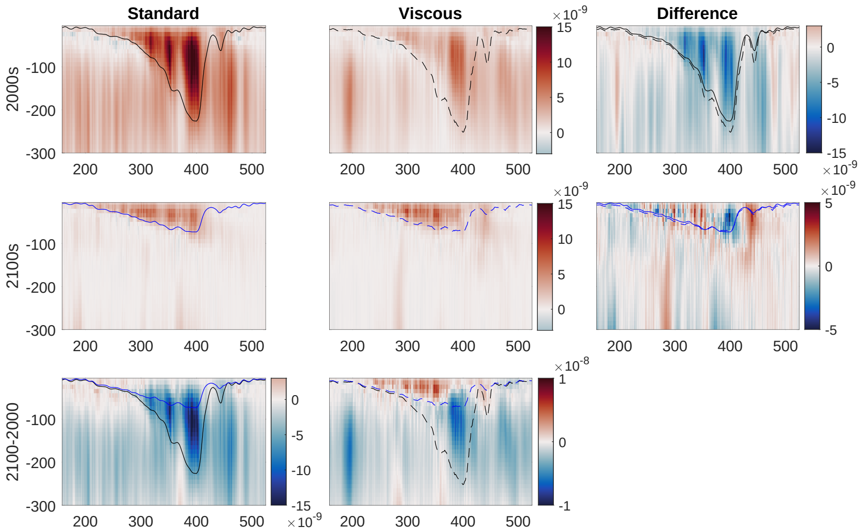


Figure S6: Vertical buoyancy fluxes from 36hr-mean w and b with spatial mean and linear trends removed. Compare with figure 10 in the main text.

the reduction in the total flux with a warmer climate of 37% for the standard cases and 32% for the viscous cases.

Results are consistent regardless of boundary conditions, with particle advective fluxes showing larger effects of both viscosity and climate than the gravitational fluxes. In the 2100s, the advective fluxes are much smaller than in the 2000s, reduced by 64.7% for the standard and 31.3% for the viscous case, and more similar, with the viscous case 5.1% larger. The submesoscale components show yet larger effects: $w'P'$ is 53.6% larger in the standard case in the warmer climate. The reductions with warming are 86% for the standard case, larger than the 64.0% in the viscous case.

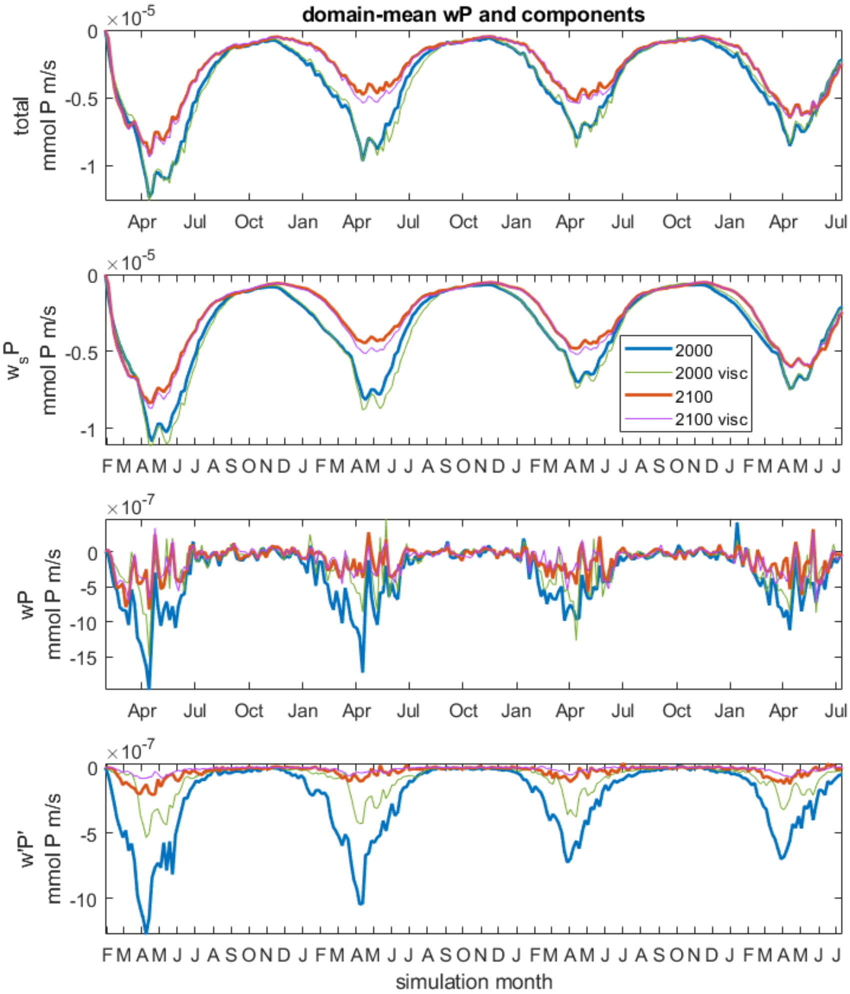


Figure S7: Vertical flux of plankton at 100m depth; mmol m/s. Top, total. 2nd row, only gravitational sinking component. 3rd row, only advective component. Bottom, submesoscale portion of advective component. In all rows, colors indicate which of 4 runs is represented, differentiating standard and viscous runs in both 2000s and 2100s climate. All simulations use $w_s = 5md^{-1}$ and $\tau = 50$days. Compare with figure 8 in the main text.

## References

Brett, G. J., Whitt, D. B., Long, M. C., Bryan, F., Feloy, K., & Richards, K. J. (2021). Sensitivity of 21st-century projected ocean new production changes to idealized biogeochemical model structure. *Biogeosciences Discussions*, 1–32.

Kay, J., Deser, C., Phillips, A., Mai, A., Hannay, C., Strand, G., ... others (2015). The community earth system model (cesm) large ensemble project: A community resource for studying climate change in the presence of internal climate variability. *Bulletin of the American Meteorological Society*, *96*(8), 1333–1349.

Large, W. G., & Yeager, S. G. (2004). *Diurnal to decadal global forcing for ocean and sea-ice models: The data sets and flux climatologies* (Vols. TechnicalReport TN-460+STR).

Richards, K. J., Whitt, D. B., Brett, G. J., Bryan, F. O., Feloy, K., & Long, M. C. (2021). The impact of climate change on ocean submesoscale activity. *Journal of Geophysical Research: Oceans*, *126*(5), e2020JC016750.